The Impact of Seasonality on Deterministic Dynamics and Noise Forcing

Alexandra Narcisse Vizcarra

A thesis submitted in partial fulfillment of

the requirements for the degree of

Master of Science

(Atmospheric and Oceanic Sciences)

at the

University of Wisconsin-Madison

May 2026

Abstract

The Impact of Seasonality on Deterministic Dynamics and Noise Forcing

by Alexandra Narcisse Vizcarra

The El Niño / Southern Oscillation (ENSO) is a dominant mode of interannual variability and a key source of seasonal climate predictability. ENSO exhibits strong seasonality and diversity; events peak in boreal winter and are weakest in boreal spring, and show significant spatio-temporal variation in their evolution. This seasonal behavior arises from both deterministic dynamics tied to the initial state and from time-varying stochastic forcing (or noise) that can initiate or disrupt event development. A comparison between a standard Linear Inverse Model (LIM) and a Cyclostationary Linear Inverse Model (CSLIM) will be investigated to disentangle how seasonality affects the interpretation of deterministic and stochastic processes in shaping ENSO evolution.

This study also aims to further diagnose the physical processes responsible for "noise" forcing. Time series of the observed noise forcing were derived, and ENSO noise forcing was calculated using optimal growth patterns in the LIM and CSLIM. Forward integration of the models with restricted noise forcing confirmed that noise during certain months were crucial for certain ENSO events. Finally, spatial structures of the noise were obtained via linear regression against atmospheric variables (e.g., sea level pressure, surface winds), demonstrating physical consistency.

Altogether, this study provides a seasonally consistent framework for separating deterministic evolution from stochastic forcing in ENSO, offering new insight into the timing, structure, and predictability of ENSO event development.

Acknowledgements

I first want to thank the man, the myth, the legend himself Dan, AKA DJ Vimont; for being an amazing advisor, for all the Dan lore, the impromptu Indie trips, and most importantly for giving me a chance in his research group. Thank you to my committee members Hannah Zanowski and Mayra Oyola for overall being amazing people, and for all the yap sessions and advice when I needed it. And thank you to Angela Rowe for allowing me to be an honorary member of your lab! I also would like to extend my thanks and appreciation to my collaborators: Erin Thomas, Matt Newman, and Melissa Breeden for all of their insightful feedback on this project.

I have so made many friends and meaningful connections here at AOS, and I couldn't have made it without them. Thank you to my labmates: Jack, Jaf, Katie, Noah, and Sagar for all the fun group meetings we had. By extension, thank you to those I've met on the 11th floor for making me feel so welcome- especially to Rudra, Evan, Nicolas, and Leo (+ Prem who's like an honorary 11th floor member) for their thoughtful insights on my research and for all the fun conversations we had. Thank you to the girls AKA my day ones: Shane, Idamis and Sofia. To Shane for all the laughs and for being someone to practice my Tagalog with. To Idamis for being the most caring, hardworking, and down to earth person I know. And to Sofia for the coffee runs, for being my gym buddy, for rooming with me at conferences, and most importantly for sticking with me through thick and thin. I would not have survived my first year of grad school without you guys < 3

I also want to express my love and gratitude to my friends both inside and outside AOS: Thank you to Ben, my favorite old person in the department- you're always the first person I think about when I look at frozen vegetables and milk at the store. Thank you to Giselle for the daily carpools, the coffee stops, our fry cone dinners, our shopping sprees, and for being a menace in DnD. And of course, thank you to Ian, mi bestie: for being the best part about Fridays, for all the adventures we had, for all the different

cuisines you had me try, for making all the delicious and amazing desserts, and for ALSO being a menace in DnD.

Thank you to Kate who always supports me through the best times and the hard times, for the unconditional love, and for being the best editor of my papers. Thank you to my beloved birds: Roki and Elvis. I know both of them can't read but I thank and love their presence despite the screaming. Thank you to my family- my dad, my mom, and two sisters: Amber and Audrey who have always believed in me. And of course, thank you to the rest of my family and friends back in the Bay Area who cheered me on. xx

Contents

List of Figures

Chapter 1

Introduction

1.1 El Niño / Southern Oscillation

The El Niño / Southern Oscillation (ENSO) is the dominant mode of interannual climate variability in the world (Philander (1990), McPhaden et al. (2006)). It is an atmospheric-oceanic coupled mode that occurs in the tropical Pacific. The atmospheric component is the Southern Oscillation, which can be best described as an interannual "see-saw" of sea level pressure (SLP) between the east and west Pacific (Wang et al. (2017)), which was coined and studied by Sir Gilbert Walker (Walker (1925)). The oceanic component to ENSO is the large scale warming (or cooling) of tropical sea surface temperatures (SST) in the Pacific (Wang et al. (2017)), first discovered by Peruvian fishermen (Enfield (1989), Murphy (1923), Murphy (1926)).

The earliest publications that develop the idea of ENSO date back to Brooks and Braby (1921), where they developed the idea of a relationship between the easterlies and rainfall in the equatorial Pacific. Three years later, Walker (1925) described the broad-scale characteristics of the Southern Oscillation in terms of sea level pressure (SLP), surface temperature, and rainfall variability. The linkage between Brooks and Braby (1921) and Walker (1925)'s work on the Southern Oscillation was made by Leighly (1933) nearly a decade later. Although remarkable, it had little to no impact in the field at the time (Wallace et al. (1998)).

ENSO also had a relatively weak behavior until major warming events began in the 1950s, which attracted renewed interest. Ichiye and Peterson (1963) studied the warming event in 1957, leading to the first hypothesis that ocean-atmospheric interactions determine the evolution of wind, SST, and rainfall in the equatorial Pacific. When weather satellites were introduced in the 1960s, Bjerknes (1969) integrated this technology into his research, where he identified coupled ocean-atmosphere interactions in the equatorial Pacific as the source of ENSO-related climate variability (Wallace et al. (1998)), and provided foundational understanding to how researchers know ENSO today. However, how the coupled system could evolve from a cold state to a warm state had remained unanswered, since there was a lack of coupled modeling capability, as well as a primitive understanding of ocean dynamics. Despite the limitations of the technology of its time, Bjerknes' work stimulated numerous observational studies, and as a result of his work, there was an improved description of the structure and evolution of ENSO by the 1980s.

The 1982 El Niño, one of the strongest events in the 20th century, was one that took the globe by surprise, and was crucial for future research on ENSO prediction. This event developed rapidly and unexpectedly (Gill and Rasmusson (1983)), and highlighted major limitations in observing the tropical Pacific and forecasting. This event served as a key motivation for the Tropical Ocean–Global Atmosphere (TOGA) program (Wallace et al. (1998)), which aimed to improve ENSO monitoring, theory, and prediction through coordinated international observations and modeling efforts.

Since TOGA, ENSO has continued to be a big focus of climate research due to its global impacts (Trenberth et al. (1998)). Advances in observations and coupled modeling have led to major improvements in understanding and forecasting ENSO, and modern research now spans topics ranging from tropical dynamics and air–sea coupling to teleconnections, predictability, and climate change influences. However, ENSO remains challenging to represent across models (Deser et al. (2012), Capotondi et al. (2015)), particularly in terms of its seasonal phase-locking, event diversity, and external forcing. These challenges motivate the continued use of simplified dynamical frameworks (e.g., Hasselman (1976), Penland and Sardeshmukh (1995), Penland and Matrasova (1994)) that can isolate key physical processes and provide insight into ENSO evolution and development.

1.1.1 ENSO Dynamics

One key feature of ENSO is its interannual variability of 2-7 years, where events peak in boreal winter time and are weakest in boreal spring (Deser et al. (2012), Capotondi et al. (2015)) and can be shown in Fig. 1.1. ENSO's interannual variability can be explained by

a variety of theories. A popular theory is the delayed oscillator theory, first proposed by Suarez and Schopf (1988), then later modeled by Battisti (1988), and Battisti and Hirst (1989). The delayed oscillator considers the effect of equatorially trapped Kelvin and Rossby wave propagation on ENSO events. The positive atmospheric-oceanic feedback that occurs in the equatorial eastern Pacific leads the SST into a warming state, or an El Niño (Wang et al. (2017)). Wind stress anomalies that are largely confined to the central and eastern basin generate Rossby waves that propagate westward (Battisti (1988)). The Rossby waves hit and reflect off the western boundary of the ocean basin, and become eastward propagating upwelling Kelvin waves. The upwelling Kelvin waves reverse the warm SST anomalies once they hit the eastern boundary of the basin, "shutting off" the El Niño event, therefore providing a negative feedback for ENSO to oscillate.

A few other theories of ENSO include: the recharge oscillator (poleward/equatorward heat transport; Wyrtki (1975), Wyrtki (1985)), the Western Pacific oscillator (cyclones/anticyclones initiated by wind stress; Wang et al. (1999)), and the advective-reflective oscillator (warm pool displacement; Picaut et al. (1997)).

The development of an El Niño event is due to a positive feedback loop between the atmosphere and the ocean (Zebiak and Cane (1987), Neelin et al. (1998)). Easterly trade winds in the central and western equatorial Pacific weaken which produces downwelling Kelvin waves that deepen the thermocline in the central and eastern equatorial Pacific. As the thermocline deepens, upwelling brings warmer deep water to the surface, leading to the warming of SSTs across the central and eastern Pacific. This warming of SSTs

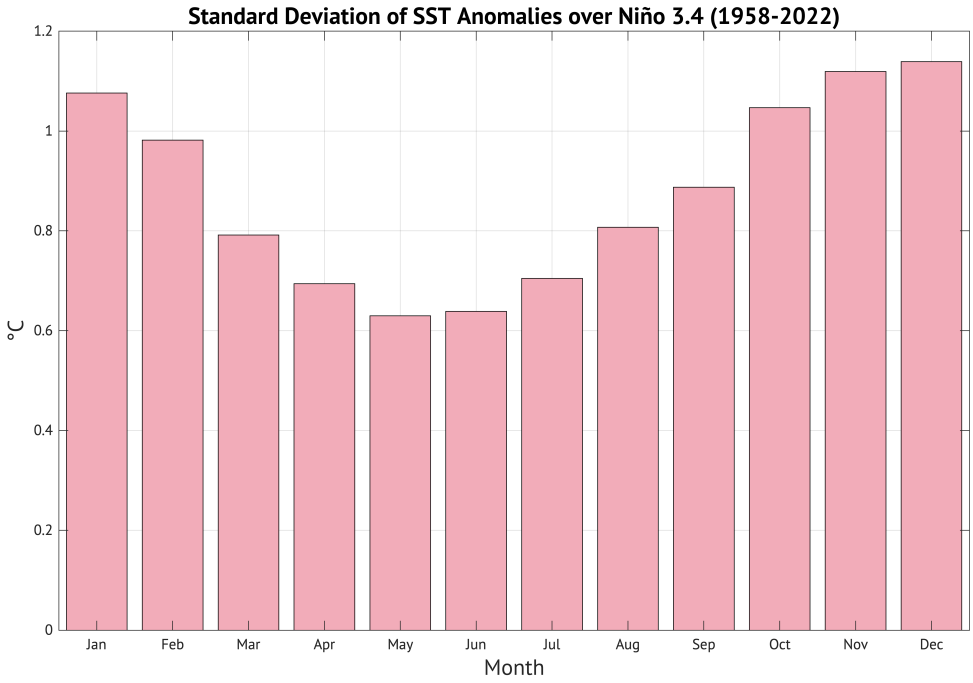

FIGURE 1.1: Standard deviation of SST anomalies over the Niño 3.4 region. Highest SST amplitude occur during boreal winter (November-January), and lowest SST amplitude occur during boreal spring (April-June).

causes the Walker circulation to weaken and shift eastward, enhancing the relaxation of the trade winds that were responsible for the warming in the first place.

Conversely, development of a La Niña can be described opposite to that of an El Niño. The easterly trade winds strengthen, which lead to a downwelling Kelvin wave, deepening the thermocline and upwelling in the eastern Pacific. This leads to colder SST anomalies in the eastern equatorial Pacific and strengthened easterly trades, completing the positive feedback.

1.2 Research Objectives

Although ENSO is a well studied phenomena, there are aspects of it that require further research. Previous literature such as Wyrtki (1975) and Capotondi et al. (2015) state that "no two ENSO events are the same" and that ENSO exhibits different spatial patterns, such as Eastern (EP) and Central (CP) Pacific patterns (Ashok et al. (2007), Takahashi et al. (2011)). This diversity suggests that there are multiple mechanisms that may contribute to ENSO development and evolution. Thomas et al. (2018) investigated the role of stochastic noise forcing in exciting different ENSO events using a linear inverse model (LIM). Their results yield that the noise forcing can play a critical role in shaping ENSO variability, motivating further investigation into how this forcing interacts with deterministic dynamics.

This study follows Thomas et al. (2018) by further examining ENSO dynamics using a LIM, and comparing the results to a cyclostationary LIM (CSLIM). One big limitation to their study is that they used a stationary LIM that contains no seasonal dynamics, yet ENSO dynamics evolve around the seasonal cycle. The first part of this study will focus in evaluating how well the models capture ENSO's deterministic development, and also investigating how much of the development is due to noise. The latter half of this study will be primarily investigating the role of noise forcing in ENSO development from both the LIM and CSLIM. In particular, this study will examine the spatial structure of the noise associated with ENSO development, with the goal of identifying noise patterns that will optimally excite ENSO variability. The influence of noise is also examined across

different ENSO events to assess its relative importance, and how its impact may differ between event types, which contribute to ENSO variability and diversity.

Chapter 2

Methods & Data

2.1 Methods

2.1.1 Linear Inverse Model (LIM)

The Linear Inverse Model (LIM) is a stochastic-dynamical framework that estimates the linear approximation to a fully nonlinear dynamical system (Penland and Sardeshmukh (1995)).

$$\frac{d\boldsymbol{x}}{dt} = \boldsymbol{L}\boldsymbol{x} + \boldsymbol{\zeta} \tag{2.1}$$

where $\boldsymbol{x}$ is the state vector that contains variable inputs (eg: SST, SSH, etc.), $\boldsymbol{L}$ is the dynamical systems matrix that contains the linear approximation to the deterministic dynamics, and $\boldsymbol{\zeta}$ is the noise forcing term.

Under 2.1, a solution to the LIM (Chang et al. (2003)) can be obtained as

$$\mathbf{x}(t+\tau) = e^{\mathbf{L}\tau}\mathbf{x}(t) + \int_t^\tau e^{\mathbf{L}(t-s)}\boldsymbol{\zeta}(s)ds \tag{2.2}$$

where the first term on the right hand side is called the "predictable" term and the second term is the "unpredictable" term (Thomas et al. (2018)). The first term on the RHS of 2.2, which is the homogeneous solution to 2.1, can be further expressed as

$$\begin{aligned} \boldsymbol{x}(t+\tau) &= e^{\boldsymbol{L}(\tau-t)}\boldsymbol{x}(t) \\ &= \boldsymbol{G}(\tau)\boldsymbol{x}(t) \end{aligned} \tag{2.3}$$

where $\boldsymbol{G}$ is the propagator matrix that evolves to the final state $\boldsymbol{x}(t+\tau)$ from an initial condition $\boldsymbol{x}(t)$ (Penland and Sardeshmukh (1995), Penland and Matrasova (1994)). In addition, $\boldsymbol{L}$ and $\boldsymbol{G}$ can be obtained from 2.3 by using the lag-0 and lag-τ covariance matrices where

$$\boldsymbol{G}(\tau) = \boldsymbol{C}(\tau)\boldsymbol{C}(0)^{-1} \tag{2.4}$$

and

$$\begin{aligned} \boldsymbol{L} &= \frac{\boldsymbol{C}(\tau)\boldsymbol{C}(0)^{-1}}{\tau} \\ &= \frac{ln(\boldsymbol{G}(\tau))}{\tau} \end{aligned} \tag{2.5}$$

Once $\boldsymbol{L}$ and $\boldsymbol{G}$ are defined, the spatial structure of the noise term $\boldsymbol{\zeta}$ can be determined by its covariance $\boldsymbol{Q}$ where $\boldsymbol{Q} =< \boldsymbol{\zeta}\boldsymbol{\zeta}^T >$ (Penland and Sardeshmukh (1995), Penland and

Matrasova (1994)).

$$\boldsymbol{Q} = -(\boldsymbol{L}\boldsymbol{C}(\boldsymbol{0}) + \boldsymbol{C}(\boldsymbol{0})\boldsymbol{L}^{\boldsymbol{T}}) \tag{2.6}$$

This is because stationary statistics is assumed and this can be explained via the fluctuation-dissipation relation where

$$\frac{d\boldsymbol{C}(\boldsymbol{0})}{dt} = \boldsymbol{L}\boldsymbol{C}(\boldsymbol{0}) + \boldsymbol{C}(\boldsymbol{0})\boldsymbol{L}^{\boldsymbol{T}} + \boldsymbol{Q} = 0 \tag{2.7}$$

2.1.2 Cyclostationary Linear Inverse Model (CSLIM)

The CSLIM is an extended version of the LIM where the model includes the seasonally varying deterministic dynamics and noise forcing of a climate system (Shin et al. (2021)). Mathematically it can be expressed similar to the LIM:

$$\frac{d\boldsymbol{x}}{dt} = \boldsymbol{L_i}\boldsymbol{x} + \boldsymbol{\zeta_i} \tag{2.8}$$

where $i = 1, 2, ..., 12$ denoting the calendar months. In Shin et al. (2021), there are two ways to estimate the dynamical systems matrix $\boldsymbol{L_i}$: the "phased-average" approach and the "fixed-phase" approach. This paper will follow the "fixed-phase" approach where $\boldsymbol{L_i}$ can be estimated similarly to 2.5

$$\boldsymbol{L_i} = \frac{ln[\boldsymbol{C}_i(1)\boldsymbol{C}_i(0)^{-1}]}{\tau} \tag{2.9}$$

where $\boldsymbol{C_i(1)}$ and $\boldsymbol{C}_i(0)$ are the lag-1 and lag-0 covariance matrices of $\boldsymbol{x}$ for each month i, retaining the correct annual phase of the inputs of the state vector. From here, the propagator matrix $\boldsymbol{G_i}$ over time τ can be expressed as

$$\boldsymbol{G_i}(\tau) = \boldsymbol{G_{i+\tau-1}}...\boldsymbol{G_1}\boldsymbol{G_{12}}...\boldsymbol{G_i} \tag{2.10}$$

where $\boldsymbol{G_i} = \boldsymbol{C_i}(1)\boldsymbol{C}_i(0)^{-1}$, which are twelve 1-lag and 0-lag covariance matrices, and the subscript for each $\boldsymbol{G_i}$ is modulo 12 (Vimont et al. (2022)).

Once $\boldsymbol{L_i}$ and $\boldsymbol{G_i}$ are obtained, the noise covariance matrix $\boldsymbol{Q_i}$ can also be determined via the fluctuation-dissipation relation by discretizing the time tendency of the covariance matrix:

$$\boldsymbol{Q}_i = \frac{\boldsymbol{C}_{i+1}(0) - \boldsymbol{C}_{i-1}(0)}{2\Delta t} - (\boldsymbol{L}_i\boldsymbol{C}_i(0) + \boldsymbol{C}_i(0)\boldsymbol{L}_i^T) \tag{2.11}$$

2.1.3 Optimal Growth

Optimal growth in ENSO events can be investigated using the LIM / CSLIM by calculating the optimal initial conditions that can grow toward a particular event (Vimont et al. (2014)). Using the homogeneous solution 2.3 from 2.1, we seek the structures that grow from an initial condition $x(0)$ to a final condition $x(\tau)$ over a time period τ:

$$\begin{aligned} \boldsymbol{x}(\tau) &= e^{\boldsymbol{L}\tau}\boldsymbol{x}(0) \\ &= \boldsymbol{G}(\tau)\boldsymbol{x}(0) \\ &= \boldsymbol{G}_\tau\boldsymbol{x}(0) \end{aligned} \tag{2.12}$$

Growth $\mu(\tau)$ is defined to be the norm of $x(\tau)$ over the norm of $x(0)$:

$$\begin{aligned}\mu(t) &= \frac{||\boldsymbol{x}(\tau)||_N^2}{||\boldsymbol{x}(0)||_M^2} \\ &= \frac{\boldsymbol{x}(\tau)^T N \boldsymbol{x}(\tau)}{\boldsymbol{x}(0)^T M \boldsymbol{x}(0)} \\ &= \frac{\boldsymbol{x}(0)^T \boldsymbol{G}_\tau^T N \boldsymbol{G}_\tau \boldsymbol{x}(0)}{\boldsymbol{x}(0)^T M \boldsymbol{x}(0)}\end{aligned} \tag{2.13}$$

where M and N are the initial and final norms respectively. In this study, the L2 norm is used as a reference norm, defined as $||\boldsymbol{x}||^2 = \boldsymbol{x}^T\boldsymbol{x}$, which corresponds to the total variance of the state vector in Euclidean space (Penland and Sardeshmukh (1995), Vimont et al. (2014)). In this case, the norm matrices reduce to the identity matrix I (i.e., $M = N = I$), such that growth is measured by the amplitude of the state vector. So maximum growth occurs when the initial state $x(0)$ is aligned with the leading eigenvector (λ), solving the generalized eigenvalue problem:

$$\begin{aligned}\boldsymbol{G}^T\boldsymbol{N}\boldsymbol{G}\boldsymbol{p} - \lambda\boldsymbol{M}\boldsymbol{p} = 0 \\ \boldsymbol{G}^T\boldsymbol{N}\boldsymbol{G}\boldsymbol{p} = \lambda\boldsymbol{M}\boldsymbol{p}\end{aligned} \tag{2.14}$$

where p is the optimal initial conditions that maximize growth over time τ.

2.1.3.1 CP & EP ENSO Events & Their Optimal Growth

ENSO events can be classified as Eastern (EP) and Central (CP) Pacific ENSO events (Ashok et al. (2007), Takahashi et al. (2011), Capotondi et al. (2015)) based on the

location of maximum warming along the equator. EP ENSO events exhibit maximum warming in the eastern equatorial Pacific, and CP ENSO exhibit maximum warming in the central equatorial Pacific.

Takahashi et al. (2011) described the EP and CP index as a linear combination of the first two leading EOFs for SST, which can be shown in Fig. 2.1

$$EP = \frac{PC1 - PC2}{\sqrt{2}} \tag{2.15}$$

$$CP = \frac{PC1 + PC2}{\sqrt{2}} \tag{2.16}$$

However, in our analysis, the second PC of SST characterizes the trend (which was removed in Takahashi et al. (2011)), while the third PC is more closely aligned with mode 2 from Takahashi et al. (2011). Hence, the EP (n_{EP}) and CP (n_{CP}) coordinate directions (Vimont et al. (2014)) can be defined as:

$$n_{EP} = \{\frac{1}{\sqrt{2\lambda_1}}, 0, -\frac{1}{\sqrt{2\lambda_3}}, 0, 0, ...\} \tag{2.17}$$

$$n_{CP} = \{\frac{1}{\sqrt{2\lambda_1}}, 0, \frac{1}{\sqrt{2\lambda_3}}, 0, 0, ...\} \tag{2.18}$$

where λ denotes their respective eigenvalues. The associated final norms are described as

$$N_* = n_*^T n_* + \epsilon l \tag{2.19}$$

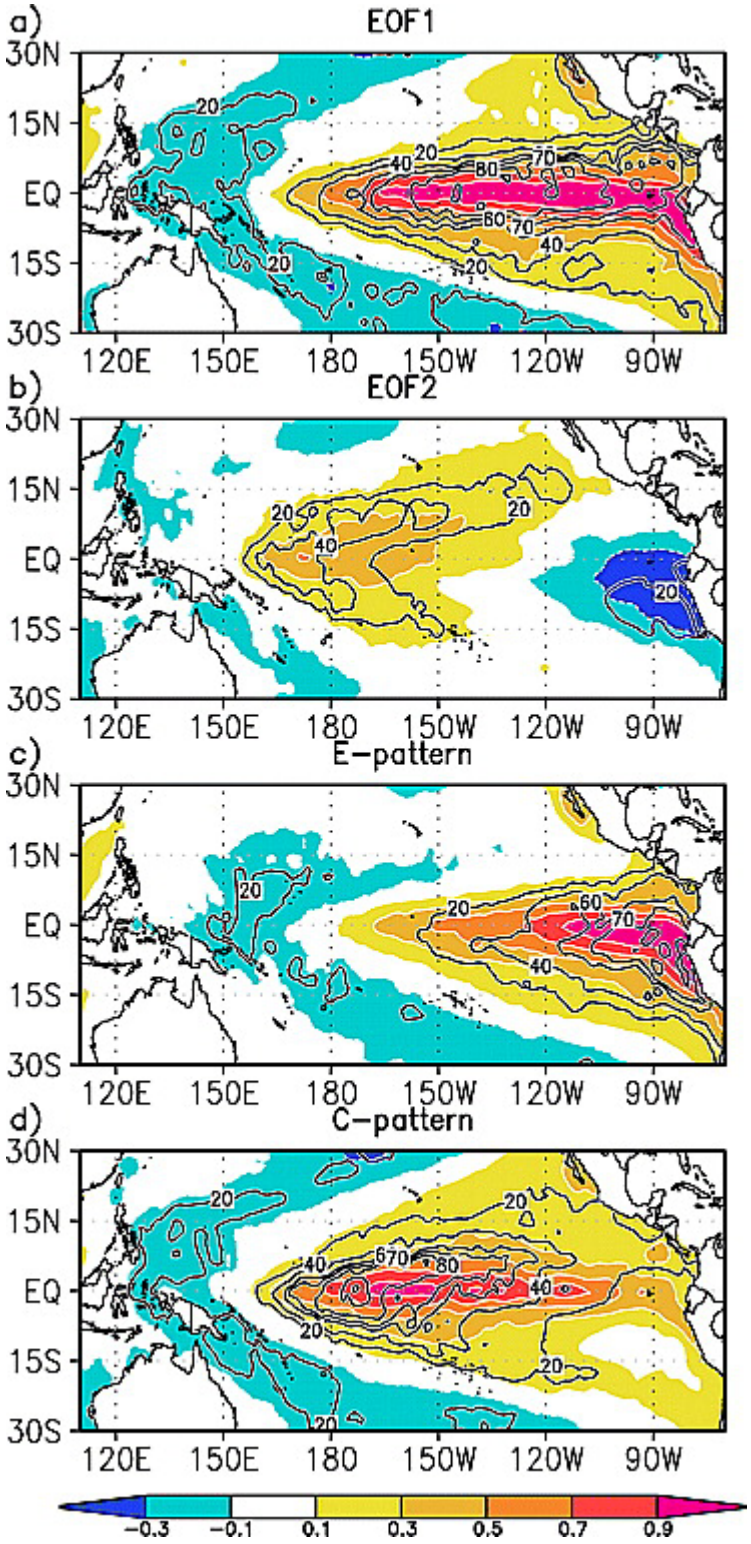

FIGURE 2.1: Linear regression coefficients (°C, shading) between the 1870–2010 HadISST sea surface temperature anomalies and PC1 (a), PC2 (b), CP index (c), and EP index (d). This is Fig. 3 from Takahashi et al. 2011.

where the * subscript can denote CP or EP, and ϵl is the identity matrix multiplied to some arbitrary small number ($\epsilon = 10^{-9}$) which is needed for numerical stability (Thomas et al. (2018), Tziperman et al. (2008)).

Like in the previous section, optimal growth conditions that grow toward a CP or EP event over a given lag τ can be calculated from 2.19 by solving the generalized eigenvalue problem (Vimont et al. (2014))

$$\begin{aligned} \boldsymbol{G}_*^T \boldsymbol{N}_* \boldsymbol{G}_* p_* - \mu_*(\tau) p_* = 0 \\ \boldsymbol{G}_*^T \boldsymbol{N}_* \boldsymbol{G}_* p_* = \mu_*(\tau) p_* \end{aligned} \tag{2.20}$$

where the subscript * on N indicates a specified final norm (CP or EP) and the subscript * on p or μ indicates that the quantity is calculated from that specified final norm. The optimal initial structure p_{CP} or p_{EP} is referred to as the CP or EP optimal, respectively. Thus, we can also determine the initial state that maximizes the deterministic growth towards a CP or an EP direction (Penland and Sardeshmukh (1995), Vimont et al. (2014), Thomas et al. (2018)). Fig. 2.2 and Fig. 2.3 show the (eg: 9 month) growth structures for the L2, CP, and EP norm for the LIM and CSLIM respectively.

2.1.4 Estimating the Noise Term

To investigate the characteristics of the noise forcing term $\boldsymbol{\zeta}$ itself, we follow the approach of Penland and Hartten (2014). More specifically, the time tendency of the state vector $\frac{d\boldsymbol{x}}{dt}$ is expressed as a centered difference which is a more accurate representation compared

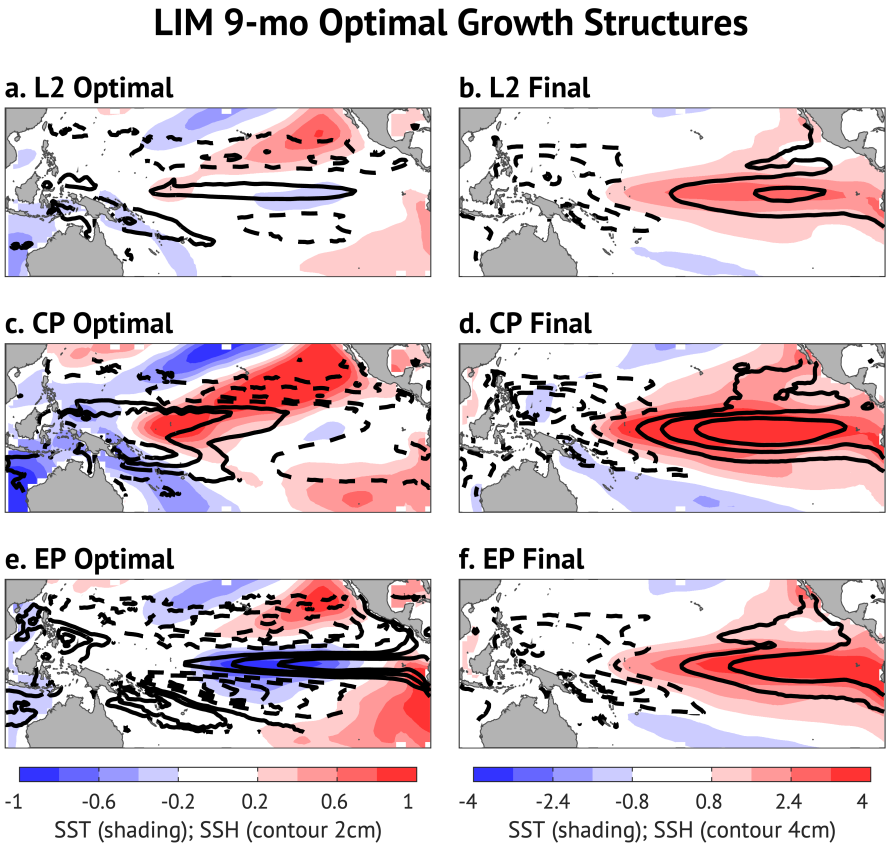

FIGURE 2.2: 9 month LIM optimal initial (left) and final (right) structures calculated from the stationary LIM for the L2 (a, b), CP (c, d), and EP (e, f) norm. Shading indicates SST, contours are SSH. Solid black contours are positive SSH anomalies, dashed black contours are negative SSH anomalies, and zero contour is omitted.

to a forward or backward difference. A centered difference approximates the derivative symmetrically around time t, which gives a more accurate estimate of $\frac{d\boldsymbol{x}}{dt}$ and avoids phase shifts that occur with forward or backwards differences.

So for the LIM, the noise is expressed as

$$\boldsymbol{\zeta} = \frac{\boldsymbol{x}(t+\Delta t) - \boldsymbol{x}(t-\Delta t)}{2\Delta t} - \boldsymbol{L}\boldsymbol{x}(t) \tag{2.21}$$

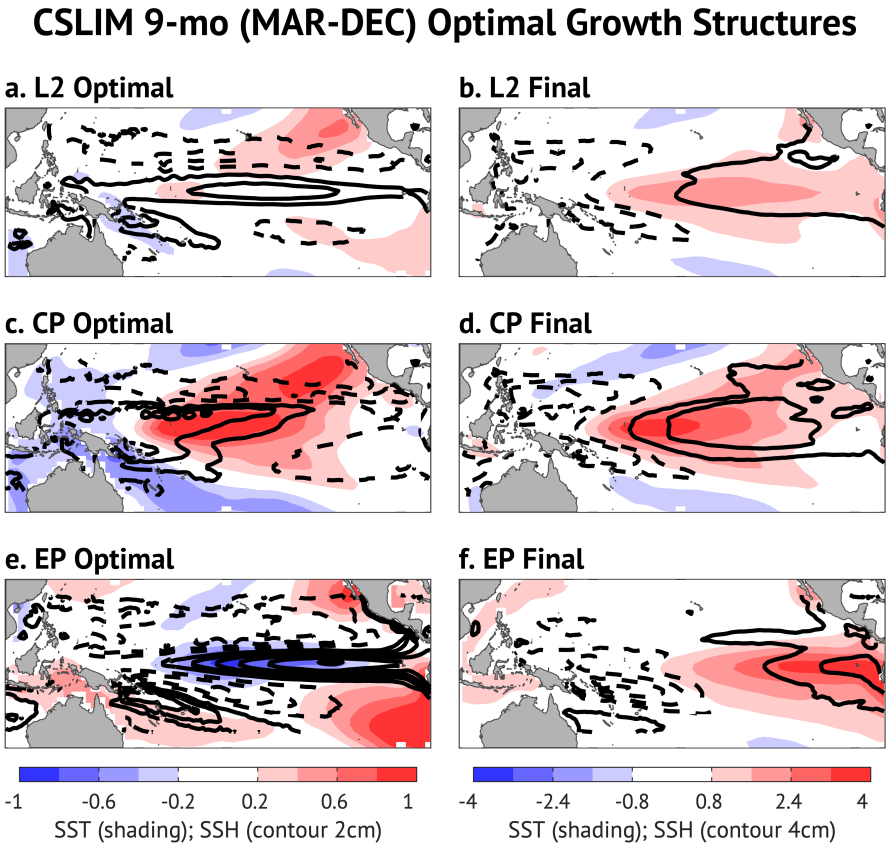

FIGURE 2.3: 9 month (March - December) optimal initial (left) and final (right) structures calculated from the CSLIM for the L2 (a, b), CP (c, d), and EP (e, f) norm. Shading indicates SST and contours are SSH. Solid black contours are positive SSH anomalies, dashed black contours are negative SSH anomalies, and zero contour is omitted.

where $\Delta t = 1$ day. For the CSLIM, it can be expressed similarly

$$\boldsymbol{\zeta_i} = \frac{\boldsymbol{x}(t+\Delta t) - \boldsymbol{x}(t-\Delta t)}{2\Delta t} - \boldsymbol{L_i}\boldsymbol{x}(t) \tag{2.22}$$

where both $\boldsymbol{\zeta_i}$ and $\boldsymbol{L_i}$ are time-dependent that correspond to the calendar month, and $\Delta t = 1$ day.

For both calculations of $\boldsymbol{\zeta}$, subtracting the deterministic tendency $\boldsymbol{Lx}(t)$ effectively removes the predictable, linear component of the system's evolution, which leaves behind the unpredictable portion of the dynamics. In this sense, the estimation of $\boldsymbol{\zeta}$ can be viewed as a dynamical filter, isolating the stochastic forcing that drives variability not captured by the linear operator (Penland and Hartten (2014), Thomas et al. (2018)). This filtered noise field provides a direct means of assessing when and where the system is most susceptible to random atmospheric perturbations.

In addition, the reason why the noise estimation should be estimated using daily data is because the LIM assumes that the noise term $\boldsymbol{\zeta}$ is temporally uncorrelated. However, if $\boldsymbol{\zeta}$ is computed using monthly data, the high-frequency variability gets smoothed out, making it autocorrelated in time. Using daily rather than monthly data therefore ensures that the estimated noise term represents fast fluctuations that are approximately white in time and consistent with the assumptions of the LIM framework.

2.1.5 Note on Noise Calculations

Equation 2.2 decomposes the evolution of the system into a linear deterministic component (first term on the RHS) and a stochastic component (second term on the RHS). In this framework, the noise term is estimated as a residual and will be used extensively in Section 3.1.

Equations 2.21 and 2.22 diagnose the noise by subtracting the linear deterministic tendency from the total tendency of the system. In this sense, the linear operator acts

as a dynamical filter, and the noise term is obtained by "backing out" the unresolved component of the dynamics, and will be used in Section 3.2.

In reality, the noise term represents the aggregate effect of unresolved processes, which include high-frequency variability and nonlinear interactions that occur on timescales shorter than those resolved by the model. These processes are therefore represented as stochastic forcing acting on the system.

2.2 Data

2.2.1 Building the State Vector: Monthly Data

The state vector for the first part of the results will be using monthly data, and the variables that will be used are SST and SSH. SST is obtained from the NOAA Extended Reconstruced Sea Surface Temperature version 5 (ERSSTv5; Huang et al. (2017) on a 1° latitude x 1° longitude grid. SSH is obtained from Oceans Reanalysis Systems 5 (ORAS5; Zuo et al. (2019)) on a 0.25° latitude x 0.25° longitude grid. The data is cosine weighted and the annual cycle has been removed over the region $30°N - 30°S$, $100°E - 285°E$ over the time period 1958-2022. Thus the full state vector is constructed as such

$$\boldsymbol{x} = \left[\frac{\boldsymbol{z}_{1-11,SST}}{\sum_{all} \sqrt{\lambda_{SST}}} \frac{\boldsymbol{z}_{1-5,SSH}}{\sum_{all} \sqrt{\lambda_{SSH}}} \right] \tag{2.23}$$

where $\boldsymbol{z}$ represents the variables by principle components (PCs), using the first leading 11 (81.8% variance explained) and 5 (63.3% variance explained) PCs are used for SST

and SSH respectively. The PCs are scaled by the square root of their total variance. The number of PCs that were chosen in the state vector were determined from the τ-test (Penland and Sardeshmukh (1995)). The reason why both SST and SSH are used in the state vector is because it allows for representation of coupled surface and subsurface processes, with SST characterizing surface variability and SSH acting as a proxy for thermocline depth and subsurface heat content essential to ENSO dynamics (Zebiak and Cane (1987), Battisti and Hirst (1989)).

2.2.2 Building the State Vector: Daily Data

For the latter half of this analysis, the state vector is constructed in the same ways using the leading 11 and 5 PCs for SST and SSH respectively; however, daily data will be used instead of monthly. SST is obtained from Optimum Interpolation Sea Surface Temperature (OISST; Huang et al. (2021)) where the data is interpolated from a 0.25° x 0.25° grid into a 2° x 2° grid. SSH is obtained from the Global Ocean Ensemble Physics Reanalysis (GLORYS12v1; Lellouche et al. (2021)) on a 0.25° x 0.25° grid. The data is cosine weighted and the annual cycle has been removed over the region $30°N - 30°S$, $100°E - 285°E$ over the time period 1993-2022.

2.2.3 Atmospheric Variables

In order to see what the noise structures look like, the projected noise optimals are regressed against various atmospheric variables. Daily data obtained from ECMWF Reanalysis (ERA5; (C3S)) from the time period 1993-2022 include mean sea level pressure

(SLP), and 10m zonal and meridional surface winds. The data is interpolated from a a 0.25° x 0.25° grid to a a 2° x 2° grid and the anomalies are calculated over the whole globe.

Chapter 3

Results

3.1 Hovmöller Diagrams

3.1.1 Composites of ENSO Events

In order to see the differences between the LIM and the CSLIM, Hovmöller analysis is used, which shows the evolution of equatorial SST. A composite analysis showing the top 10 June optimal ENSO years will first be shown in order to see how both models capture ENSO event development. The June optimal years are chosen because it precedes the development of the events, and are independent of the noise. Then, individual events will be investigated in order to determine if noise has a role in individual event development.

The top 10 June optimal El Niño years chosen for the composites are 1993, 1976, 1994, 2009, 1965, 1991, 1972, 1982, 2015, and 1997. The top 10 June optimal La Niña years

that were chosen are 1988, 1998, 2010, 1973, 1975, 1999, 1970, 2007, 2002, and 1971.

3.1.1.1 Top 10 June Optimal El Niño Years

To interpret the results, we first start by looking at what observations look like (Fig. 3.1h, p). The equatorial SST begins to warm in the spring and early summer (April-June), reaching a maximum in the winter (November-January). Then the event begins to decay in the spring and early summer (March-June) of the second year before the El Niño ends and a subsequent La Niña begins to develop.

Before investigating the LIM and CSLIM simulations, it is important to note that for each initial state, the deterministic SST anomalies (shading) plus the noise forcing (contours) equal the fully observed SST anomalies produced by the models. To guide the interpretation of these results, we focus on how the LIM and CSLIM partition ENSO evolution into deterministic growth versus noise forcing as a function of lead time. In particular, we assess when the deterministic dynamics begin to capture the observed growth and decay of ENSO events, and whether variability is attributed primarily to deterministic processes or to stochastic forcing. This provides insight into whether ENSO development is represented as an internally growing mode or as noise-driven variability within each model framework.

We begin by investigating how the LIM forecasts the event (Fig. 3.1 top row). Starting with initializing the model in January of year 1 (Fig. 3.1a), the deterministic forecast of

SST is very weak as indicated by the shading. However, there is an excessive amount of noise as indicated by the positive contours. That means when the model is initialized in January, several months before the peak of the event, the model depicts that the development is driven by noise. Now, if the LIM is initialized in March (Fig. 3.1b), the deterministic forecast shows some improvement compared to the January initialization. However, it is still an extremely weak deterministic forecast, and the noise contours still heavily dominate in contributing to event development. It is when looking at the September initial condition (Fig. 3.1e) where the deterministic forecast begins to look like observations (Fig. 3.1h). However, the noise is still heavily present in all of the LIM forecasts even if the forecast is initialized close to the peak of the event (Fig. 3.1e), meaning that according to the LIM, noise is driving event development. In addition, in the November initialization (Fig. 3.1f), the positive noise contours disappear and negative noise contours are present in the late spring to winter of the second year. This indicates that the LIM would infer that the noise is also responsible for terminating the El Niño event, so that the subsequent La Niña can begin to develop.

The CSLIM forecasts show a different partitioning between the deterministic dynamics and the noise-forced evolution. The deterministic evolution in the March initial state (Fig. 3.1j) already shows event growth, peak, and decay clearly. By the May initial state (Fig. 3.1k), the deterministic forecast looks nearly identical to observations (Fig. 3.1p); while in the LIM, it took all the way until the September initial condition (Fig. 3.1e) to capture deterministic development to that same magnitude. In addition, the noise contours in the CSLIM are not as prominent in driving event development and decay compared to

the LIM, and the noise contours almost completely disappear after the September initial condition (Fig. 3.1m).

The difference between the LIM and CSLIM is that the CSLIM contains seasonally varying deterministic dynamics, whereas the LIM does not contain such dynamics. The difference between their respective Hovmöller diagrams indicates that the LIM misrepresents ENSO's seasonally varying growth rate as noise. Furthermore, since the CSLIM includes seasonal dynamics, it was able to appropriately capture the deterministic seasonal evolution.

Overall, the results indicate that the LIM attributes a large fraction of ENSO growth to stochastic forcing, particularly at longer lead times whereas the CSLIM captures much of this growth within the deterministic dynamics. In physical terms, this likely suggests that the seasonal phase-locking of ENSO growth is not adequately represented in the LIM, which is time-invariant, and is instead aliased into the noise term. In contrast, for the CSLIM, it incorporates the seasonally varying dynamics and is able to represent this growth as an intrinsic, predictable feature of the system.

3.1.1.2 Top 10 June Optimal La Niña Years

Here, we repeat the previous analysis for the developing La Niña events. Once again, starting with examining the LIM outputs (Fig. 3.2 first row), the January (Fig. 3.2a) and March (Fig. 3.2b) initial conditions demonstrate an extremely weak deterministic

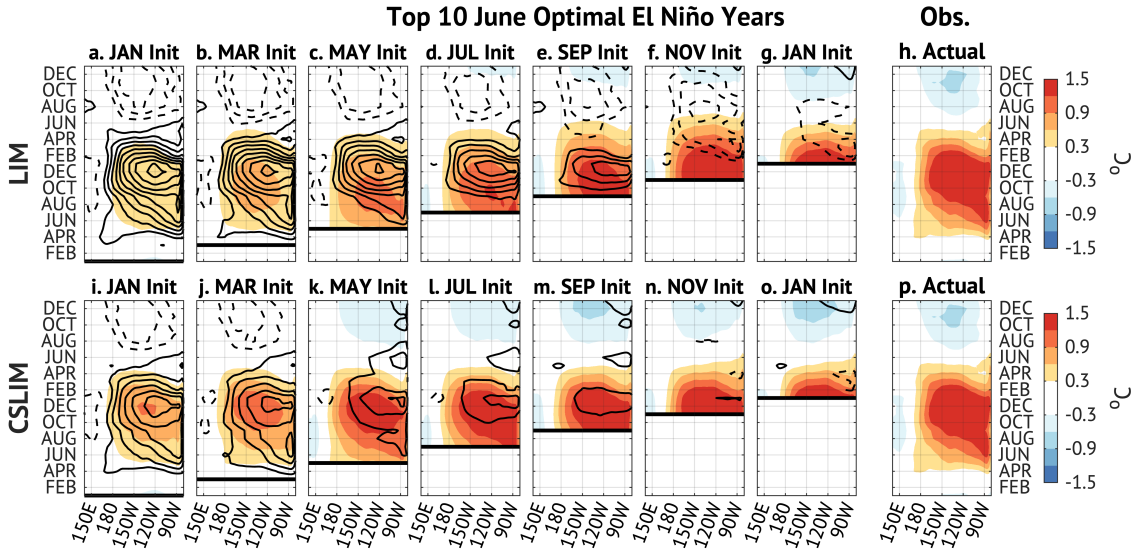

FIGURE 3.1: Hovmöller diagrams of the top 10 June Optimal El Niño years in the tropical Pacific ($30°N - 30°S$, $100°E - 285°E$). Time increases upwards along the y-axis starting in January, and longitude is shown on the x-axis. The observed SST anomalies are shown in (h) and (p). The top row indicates SST anomaly prediction from the LIM that contains the deterministic dynamics (shading) and the noise forcing (contours). The bottom row is explained similarly but for the CSLIM. The columns represent different initializations of the models every 2 months for a 2-year forecast, and are indicated by the horizontal black lines in each diagram.

forecast. The negative noise contours for both early forecasts indicate that the development of La Niña is due to noise. The May (Fig. 3.2c) and July (Fig. 3.2d) initial conditions then show that the forecast is slowly becoming more robust; however, the negative noise forcing contours are still prominent in event development. By the September initial state (Fig. 3.2e), the forecast now looks similar to observations and is able to capture the peak and decay, and the negative noise contours almost completely disappears. However, the positive noise contours in the eastern Pacific are amplified compared to the earlier forecasts. This indicates that the noise is terminating the event, even when the LIM initiates a forecast after the peak (Fig. 3.2g).

Now, in comparison with the CSLIM diagrams (Fig. 3.2 second row), the deterministic forecast looks like observations in the May initial conditions (Fig. 3.2k). In contrast, it took until the September initial condition (Fig. 3.2e) for the LIM to capture the deterministic development to the same magnitude. The negative noise contours do not contribute as much to event development compared to the LIM, and the contours even disappear almost completely in the July initial state (Fig. 3.2l). However, it is important to note that even though the CSLIM is able to capture ENSO's seasonal development, the deterministic forecast is predicting a colder event than what actually occurred.

Once again, it can be said that the LIM is aliasing La Niña's seasonal growth and decay as noise, and the CSLIM appropriately captures La Niña's seasonal evolution. In addition, there is a persistent positive noise forcing in the far eastern Pacific in all initial states for both models. This is due to nonlinearities or state dependent noise that are not captured in the LIM and CSLIM. As a result, both models alias those missing dynamics as noise.

Consistent with the El Niño composite results, the LIM tends to attribute a substantial portion of La Niña development and decay to stochastic forcing, whereas the CSLIM captures much of this evolution within its deterministic dynamics. Once again, this highlights that seasonally varying growth rates are misrepresented as noise in the LIM. The persistent noise signals in the eastern Pacific in both models further suggest the presence of nonlinear or state-dependent processes that are not captured by the linear framework and are therefore projected onto the noise term.

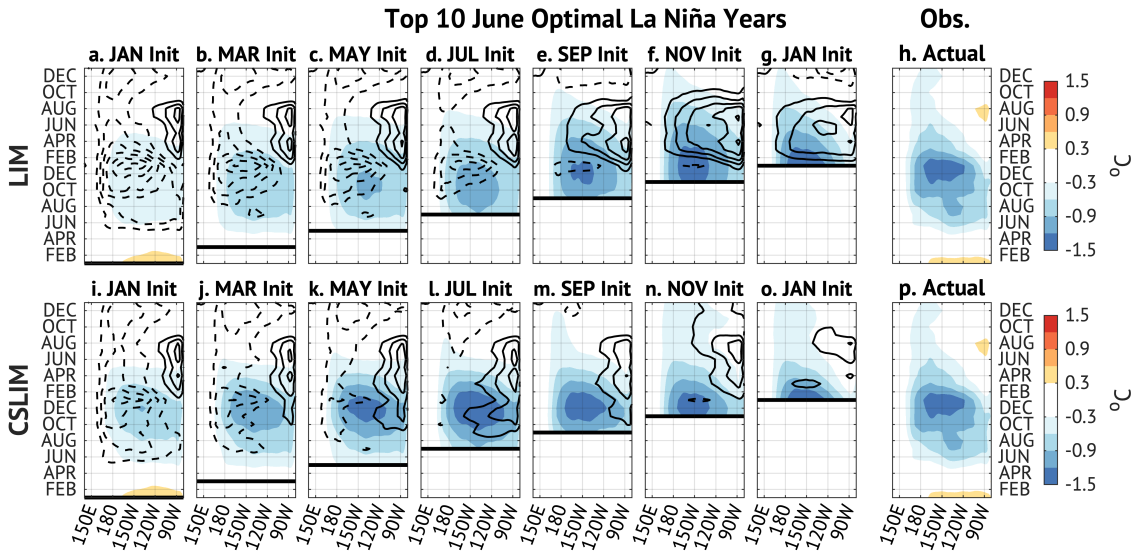

FIGURE 3.2: As in Fig. 3.1, but for the top 10 June optimal La Niña years.

3.1.2 Individual ENSO Events

We now examine individual ENSO events to better understand how the partitioning between deterministic dynamics and noise forcing varies at different cases. While the June optimal composites highlight the typical seasonal evolution of ENSO, individual events provide insight into how this balance depends on event strength, type, and background state.

3.1.2.1 2015 El Niño

It can be seen that both models are able to capture the deterministic evolution of the El Niño at longer lead times. However, the deterministic evolution is better forecasted in

the CSLIM as far back as the May initial condition (Fig. 3.3k), while the LIM goes as far back as July (Fig. 3.3d). Although this event was well forecasted by both models, it can be seen that the positive noise contours are contributing to event development in the March (Fig. 3.3j) and May (Fig. 3.3k) initial conditions, and the deterministic forecast was insufficient to produce a strong El Niño. But by July (Fig. 3.3l), the positive noise contours disappear, and the forecast for this El Niño is almost completely deterministic. That indicates that between the March and July initial state, the noise was responsible for the development of the 2015 El Niño.

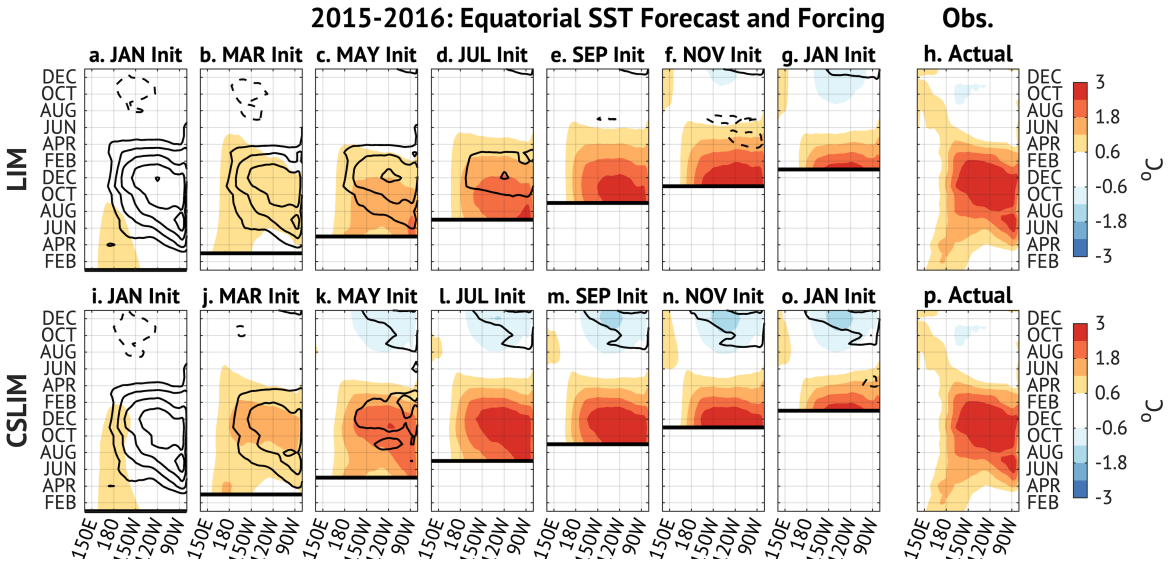

FIGURE 3.3: Hovmöllers for the seasonal evolution of the 2015 El Niño event. The description of the Hovmöllers are the same as Fig. 3.1.

Thus, the 2015 El Niño event illustrates a transition influenced from noise at early lead times to predominantly deterministic evolution closer to the event peak. This suggests that once favorable conditions are established, the 2015 event evolves as a deterministically driven mode, while earlier development is more sensitive to stochastic forcing.

3.1.2.2 1997 El Niño

The results for the 1997 El Niño can be explained in a similar way as the 2015 event. The CSLIM was able to capture the deterministic evolution as early as the May initial condition (Fig. 3.4k), and the deterministic evolution was captured as early as the July initial condition (Fig. 3.4d) for the LIM. The long predictability of the 1997 event is consistent with Thomas et al. (2018) and Newman and Sardeshmukh (2017), especially as the CSLIM was able to capture the evolution as far back as May (Fig. 3.4k). The noise after July for the LIM and May for the CSLIM does not have much impact on the development. However, the noise in the LIM (Fig. 3.4e-g) contributes to a rapid decay, and the noise in the CSLIM (Fig. 3.4m-o) is persistently warm until the subsequent La Niña. This indicates that the noise between January and May is responsible for the development of the event, and also contributes to how long the 1997 event lasted.

Similar to the 2015 event, the 1997 El Niño exhibits strong deterministic predictability at long lead times, particularly in the CSLIM. The role of noise is primarily confined to the early development stage of the event and to modulating the duration, reinforcing the idea that this strong El Niño event is largely governed by deterministic seasonal growth once initiated.

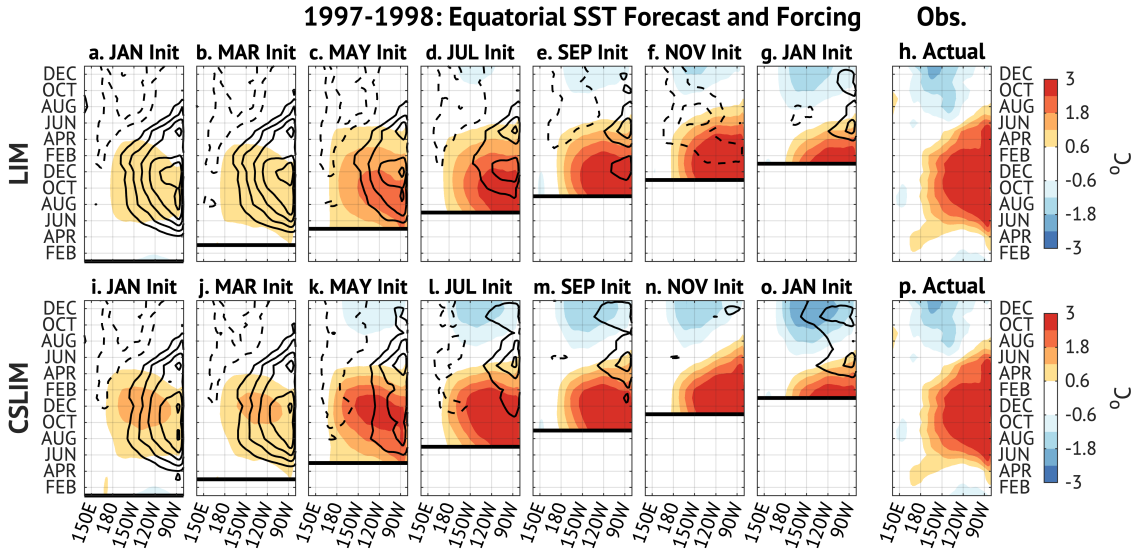

FIGURE 3.4: Hovmöllers for the seasonal evolution of the 1997 El Niño event. The description of the Hovmöllers are the same as Fig. 3.1.

3.1.2.3 1982 El Niño

Both the LIM and CSLIM simulations do a poor job at reproducing the deterministic dynamics (shading) prior to the September initial state (Fig 3.5e, m), and instead the noise forcing dominates (contours). It is when both models are initialized in September where they are able to capture the peak of the event, meaning that the state of the system during September is sufficient for generating a skillful deterministic forecast. In addition, this also means that the state of the system prior to the September initial state was insufficient in generating the El Niño event without the influence of noise, which is consistent with the results from Thomas et al. (2018).

The 1982 El Niño highlights a case where deterministic dynamics alone are insufficient to

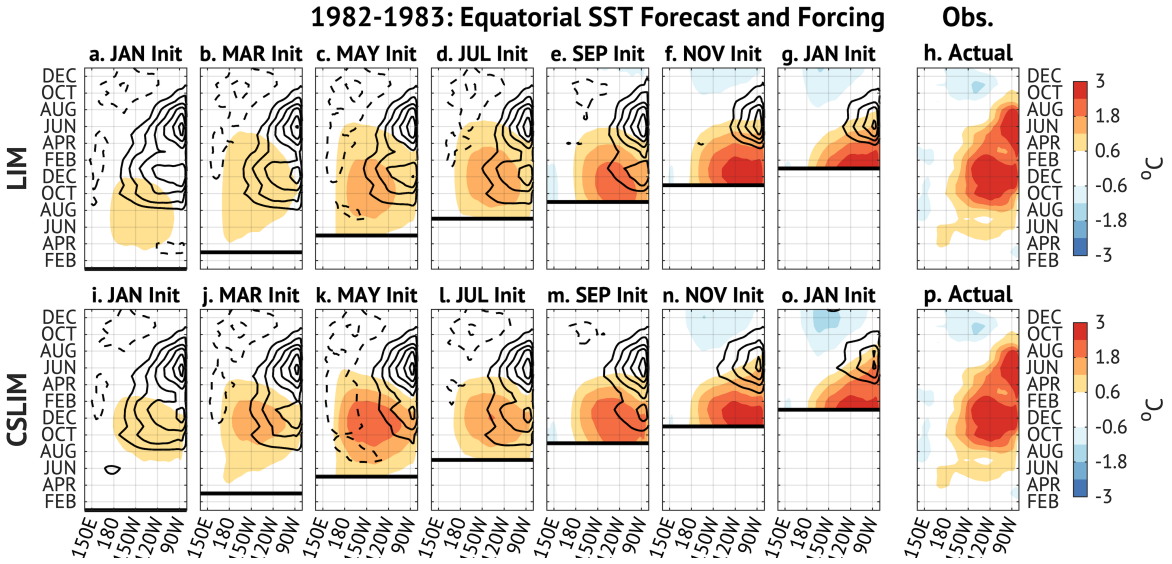

FIGURE 3.5: Hovmöllers for the seasonal evolution of the 1982 El Niño event. The description of the Hovmöllers are the same as Fig. 3.1.

generate the event at long lead times, and stochastic forcing plays a dominant role prior to boreal fall. This suggests that the preconditioning of the system was weak, requiring noise-driven perturbations to trigger the event.

3.1.2.4 2009 El Niño

The 2009-10 event is particularly interesting because it was a CP El Niño event. Both the LIM and the CSLIM do a poor job at reproducing the deterministic dynamics of the event at any lead time. At lead times prior to the event peak (Fig. 3.6a-e, i-m), the forecasts show that the noise is almost completely explained by the noise forcing. In addition, the subsequent development of the La Niña is also completely explained by the

noise forcing: the deterministic development of the subsequent La Niña is nowhere to be seen, even at initial states near the event peak (Fig. 3.6e-g, m-o).

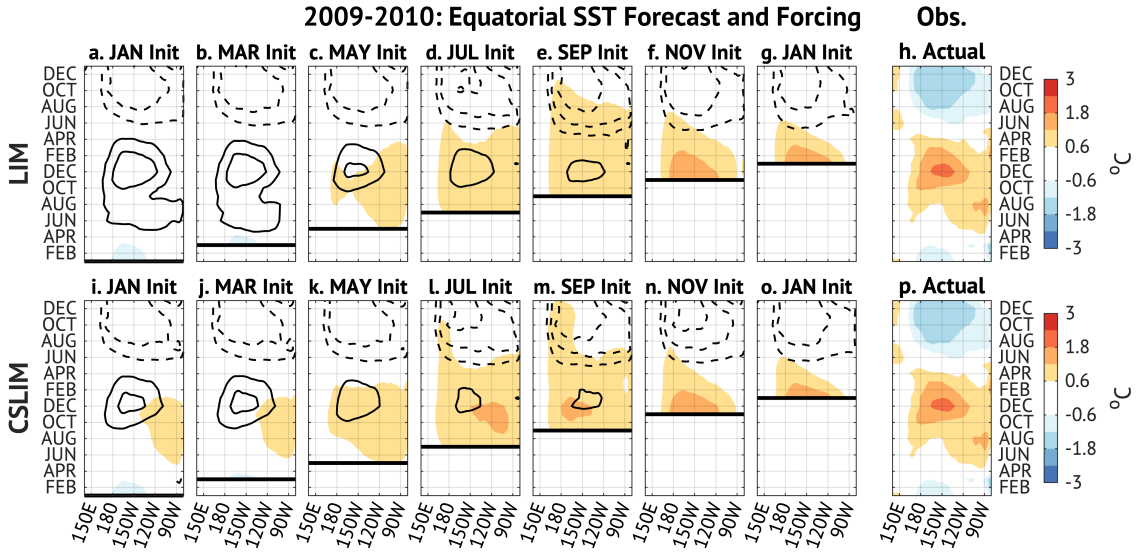

FIGURE 3.6: Hovmöllers for the seasonal evolution of the 2009 CP El Niño event. The description of the Hovmöllers are the same as Fig. 3.1.

The 2009 CP El Niño differs from the EP events (e.g. 1997, 2015), with both models attributing most of the evolution to stochastic forcing. This indicates that this CP event may be less strongly tied to deterministic seasonal instabilities and is more sensitive to nonlinearities or stochastic processes, which are not well captured within the linear deterministic framework.

3.1.2.5 1998-2000 La Niña

The 1998-2000 La Niña was a multi-year event. Starting with 1998-1999, the shading in Fig. 3.7 shows the decay of the 1997 El Niño from February to June in early initializations in both models. However, at early lead times, the LIM does a better job at capturing the deterministic dynamics of the event (Fig. 3.7 top row), while the CSLIM's deterministic dynamics predict the event to be much colder than what actually happened as indicated by the shading (Fig. 3.7 bottom row). Despite that, the CSLIM was able to accurately capture the timing of the development of the event as far back as the January initial condition. The noise forcing located on the eastern Pacific seems to balance the deterministic cold SST anomalies.

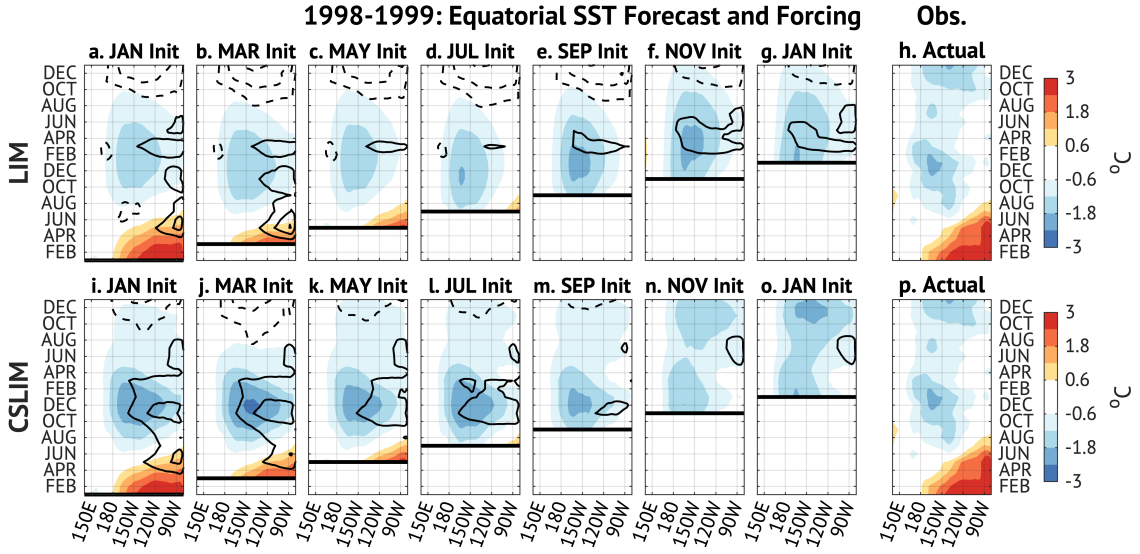

FIGURE 3.7: Hovmöllers for the seasonal evolution of the 1998 La Niña event. The description of the Hovmöllers are the same as Fig. 3.1.

The 1999-2000 event looks drastically different than the previous year's evolution. As noted in the 1998 event, the LIM was consistent in producing the deterministic dynamics at all lead times. But in the 1999 event, the LIM forecasts showed inconsistencies. At early lead times, the LIM was able to capture the end of the 1998 event, but was not able to capture the peak of the 1999 event. The skill of the LIM seems to diminish between the March (Fig. 3.8b) and September (Fig. 3.8e) initialization, and the event is driven by noise as indicated by the dashed contours during the peak. But by the November initial condition, the deterministic dynamics seem to exhibit similarities.

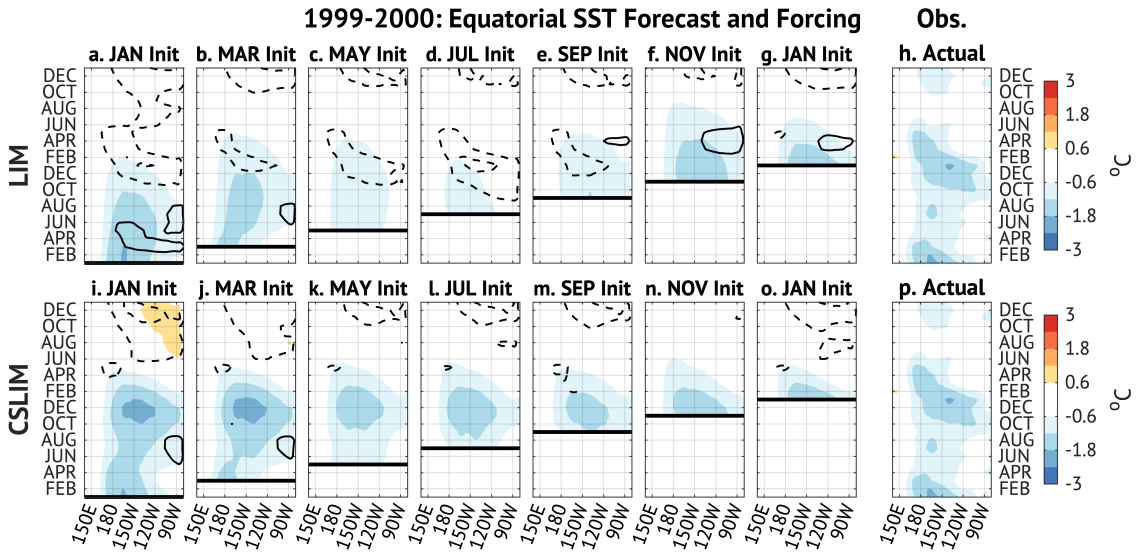

FIGURE 3.8: Hovmöllers for the seasonal evolution of the 1999 La Niña event. The description of the Hovmöllers are the same as Fig. 3.1.

Comparing to the CSLIM, the January and March initial conditions were able to capture the persisting La Niña from 1998 to 1999. However, it is important to note that the deterministic dynamics forecast the event to be colder compared to the observed. In

addition, at beginning of the May (Fig. 3.8k) initialization, the the SST anomalies in the forecast are on the same amplitude as the observed. The noise is not a dominant factor in driving event development.

Overall, following the 1997 El Niño, the LIM and CSLIM demonstrate skill in reproducing the subsequent 1998-2000 multi-year La Niña events, as evidenced by their ability to capture the timing, spatial structure, and the amplitude of SST anomalies. The CSLIM more consistently represents the temporal evolution of both the 1998 and 1999 events, although it tends to overestimate the magnitude of cold anomalies. The LIM accurately reproduces the 1998 event across lead times, but exhibits reduced skill for the 1999 event, particularly in capturing the peak amplitude and persistence of anomalies.

3.1.2.6 2010 La Niña

Early forecasts like the January (Fig. 3.9a, i) to March (Fig. 3.9b, j) initial state in both the LIM and CSLIM show that the deterministic forecast (shading) is insufficient to produce a strong La Niña, and was instead explained by the noise forcing. But, by the May (Fig. 3.9k) initial state in the CSLIM, the model was able to capture the development of the event, and the effect of noise contribution almost disappears in the forecast. As in the 2015 El Niño (Fig. 3.3), the noise forcing between the January (Fig. 3.9i) and March (Fig. 3.9j) initial states plays a key role in initiating the 2010 La Niña.

Interpretation of this result is further supported by the preceding 2009 El Niño (Fig. 3.6), which was identified as a CP event and was largely driven by stochastic forcing in both models. The noise-dominated evolution of the 2009 event suggests that the background state entering 2010 was not strongly preconditioned for deterministic La Niña development, thereby increasing the role of stochastic forcing in triggering the 2010 event.

The 2010 La Niña therefore further supports the interpretation that early-stage development can be strongly influenced by stochastic forcing, while deterministic dynamics become more dominant once the event is established. This behavior is consistent with the transition from noise-triggered growth to seasonally phase-locked evolution.

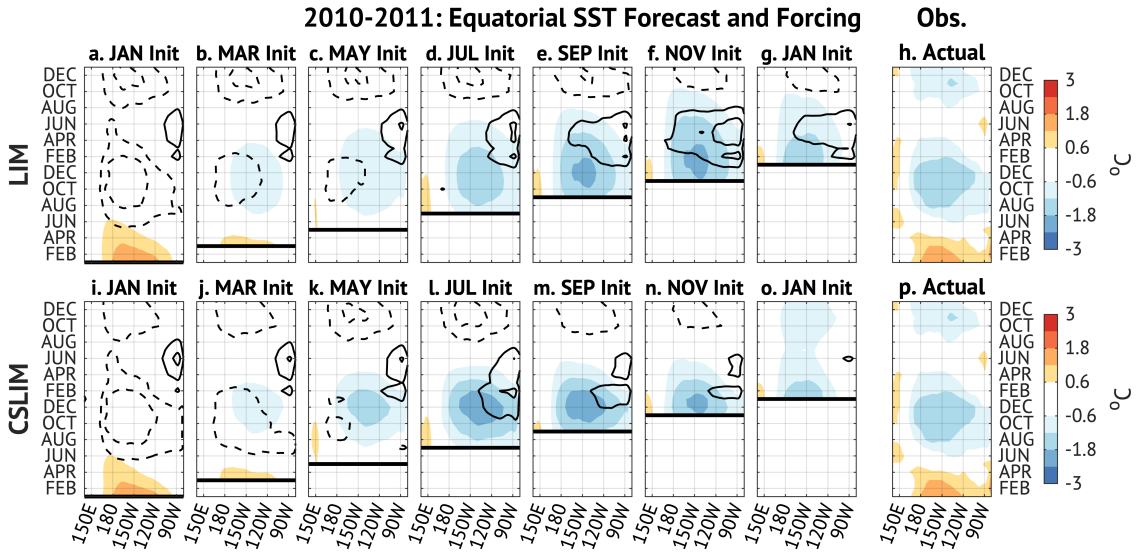

FIGURE 3.9: Hovmöllers for the seasonal evolution of the 2010 La Niña event. The description of the Hovmöllers are the same as Fig. 3.1.

Altogether, these individual events demonstrate that the relative roles of deterministic dynamics and noise forcing depend strongly on event type and initial conditions. Strong EP El Niño events, like the 1997 and 2015 event, are largely governed by deterministic seasonal growth once initiated. Whereas CP events, like the 2009 event, exhibit a greater dependence on stochastic forcing. Additionally, early-stage development across most events shows sensitivity to noise, suggesting that stochastic processes play an important role in triggering ENSO events, while deterministic dynamics govern their subsequent evolution.

3.2 Contributions of Noise to ENSO Development

3.2.1 Regression Maps

Results from the previous section show that noise has a big impact on ENSO events. This section will further investigate the noise term from both the LIM and CSLIM in order to examine the structure of atmospheric variables that may be responsible for producing noise forcing. Here, the estimated noise that is calculated in eq. 2.21 and eq. 2.22 respectively will be used for the rest of this section.

One way to see the impacts of noise is to look at the optimal initial conditions that would optimally grow towards an ENSO event. The optimals from both the LIM and CSLIM are calculated at different lags with December as the final state. The estimated noise is projected onto the L2, CP, and EP optimal in order to obtain a noise time series. By projecting the (multivariate) noise onto the optimal structures, the resulting time series

represent the noise forcing patterns that push the system toward those optimals, and hence toward eventual ENSO evolution. A 15-21 day low pass filter is then applied to the estimated noise in order to see the lower frequency variability impacts.

To look at the spatial structures of the noise, the projected estimated noise is regressed onto SLP and 10m u, v winds. Similar to Thomas et al. (2018), the regression maps are able to identify atmospheric patterns that covary with the noise forcing of these optimals.

First, let's begin by looking at the spatial regression maps of the noise from the LIM. Fig. 3.10a shows the spatial pattern in March. There is a strong North Pacific Oscillation (NPO)-type pattern present over the North Pacific ocean, depicted as a dipole of high pressure over the North Pacific and Bering Straight, and low pressure over the mid-latitude and subtropical central Pacific (Linkin and Nigam (2008)). There is also a symmetric dipole pattern present in the Southern Hemisphere, but it is relatively weaker than the NPO. And finally, there are relatively weak westerly wind anomalies present in the western equatorial Pacific.

When looking at the spatial pattern 3 months later during June (Fig. 3.10b), the NPO pattern disappears and the Southern Hemisphere has more active SLP activity similar to that of Rossby wave trains. The seasonality to the SLP anomalies are consistent with literature (e.g., Linkin and Nigam, 2008) since the NPO occurs during the boreal winter, and there is more activity in the Southern Hemisphere due to the austral winter season. In addition, the equatorial westerly wind anomalies have extended more to the central Pacific, but are still relatively weak. Finally, moving forward another 3 months later

during September (Fig. 3.10c), there is a dominant dipole of SLP located in the South Pacific, and the westerly wind anomalies are strongest during this time in the Central Pacific (You and Furtado (2018)).

Now, let's look at the spatial structures for the CP optimal. The results hold similar to the L2 optimal structures. March (Fig. 3.11a) shows the NPO structure in the Northern Hemisphere and weak equatorial westerly wind anomalies. In June (Fig. 3.11b), the NPO structure disappears, the equatorial westerly wind anomalies are less pronounced, and there is Rossby wave train activity in the Southern Hemisphere. Finally in September (Fig. 3.11c), the equatorial westerly wind anomalies continue to remain weak, but there is a dipole of SLP in the Southern Hemisphere similar to 3.10c, but on a lesser magnitude.

Finally, let's look at the spatial structures for the EP optimal. In March (3.12a), the NPO structure in the Northern Hemisphere is not present, which can be compared to the L2 (Fig. 3.10a) or CP (Fig. 3.11a) cases. The weak symmetric dipole of SLP is also present in the Southern Hemisphere. In June (3.12b), the NPO pattern has once again disappeared. There is a Rossby wave train present in the Southern Hemisphere, and a dominant low pressure signal off the coast of Chile that resembles the forcing of the south Pacific Meridional Mode in You and Furtado (2018). Equatorial westerly wind anomalies are emerging across the central Pacific. Finally in September, the equatorial westerly wind anomalies are much more prominent. In addition, the dominant low pressure system is still present off the Chilean coast, and the Rossby wave train activity is also still present in the Southern Hemisphere.

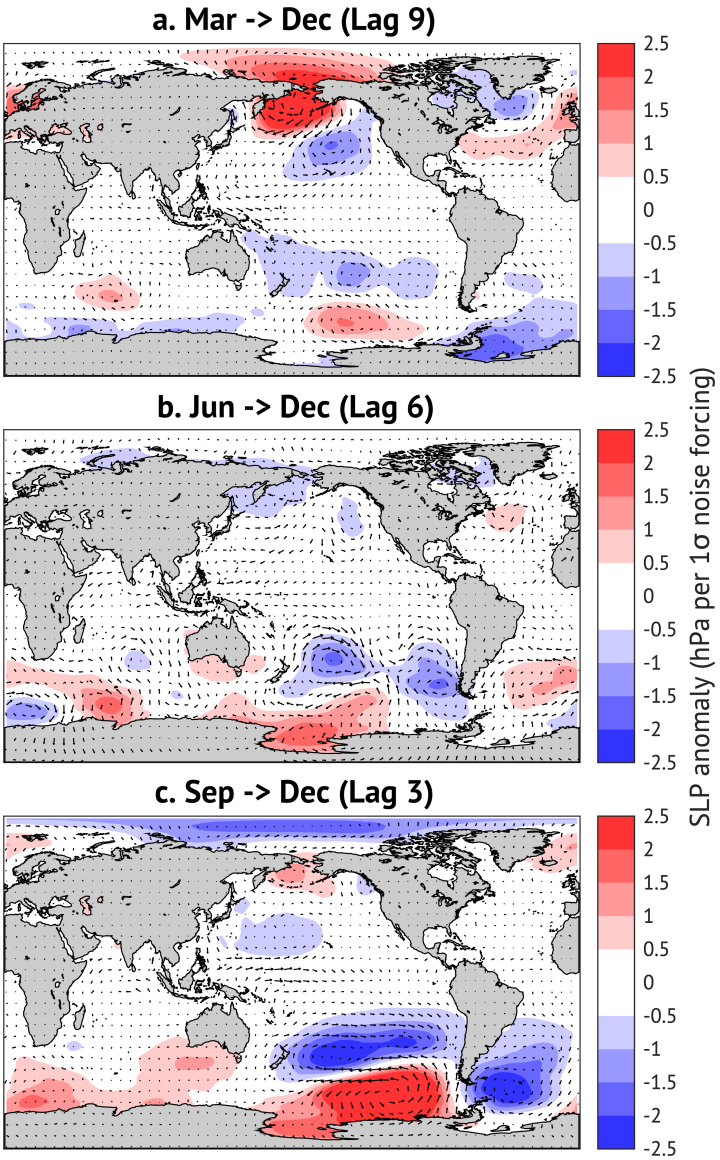

FIGURE 3.10: Spatial maps of the low pass L2-projected estimated LIM noise regressed onto SLP (contours) and 10m u and v winds (wind vectors) during (a) March, (b) June, and (c) September where December is the final state.

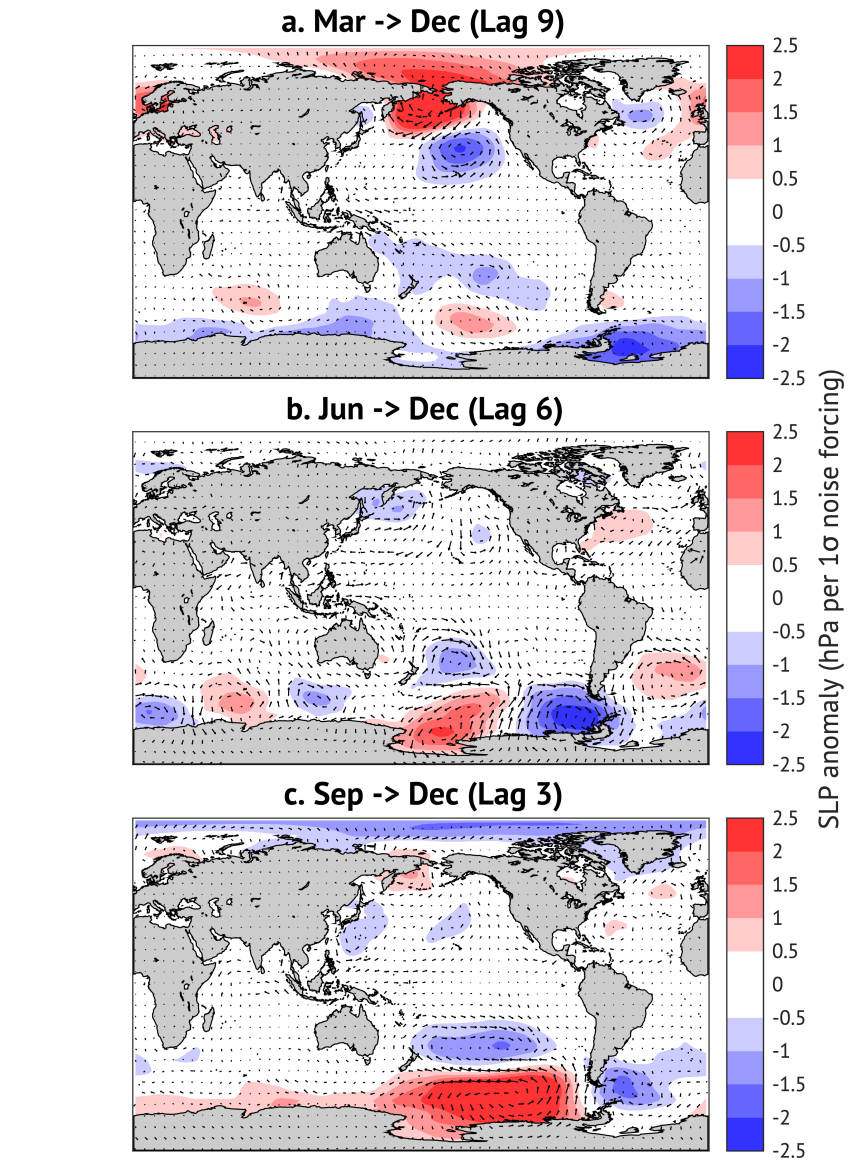

FIGURE 3.11: As in Fig. 3.10, but for the CP optimal.

To summarize, the L2 optimal appears to reflect a combination of the CP and EP optimals, which is consistent with its construction. For the CP optimal, the NPO structure is prominent during March (Figs. 3.11a), and is accompanied by the development of a South Pacific NPO-like dipole in the central South Pacific that evolves through June and into September. In contrast, the EP optimal shows little to no coherent structure in the Northern Hemisphere, particularly lacking a clear NPO signal. Instead, its evolution is characterized by the development of a South Pacific low off the coast of Chile, consistent with You and Furtado (2018), along with strong westerly wind anomalies in the equatorial Pacific during June and September. Across all optimals, the Southern Hemisphere SLP patterns share some similarities, transitioning from a relatively weak dipole in March to a more organized structure by September, resembling the South Pacific Oscillation (SPO). However, the pronounced equatorial wind anomalies—especially in the central Pacific—raise the question of whether these signals represent noise or are instead an aliasing of seasonal dynamics, as suggested by the Hovmöller diagrams.

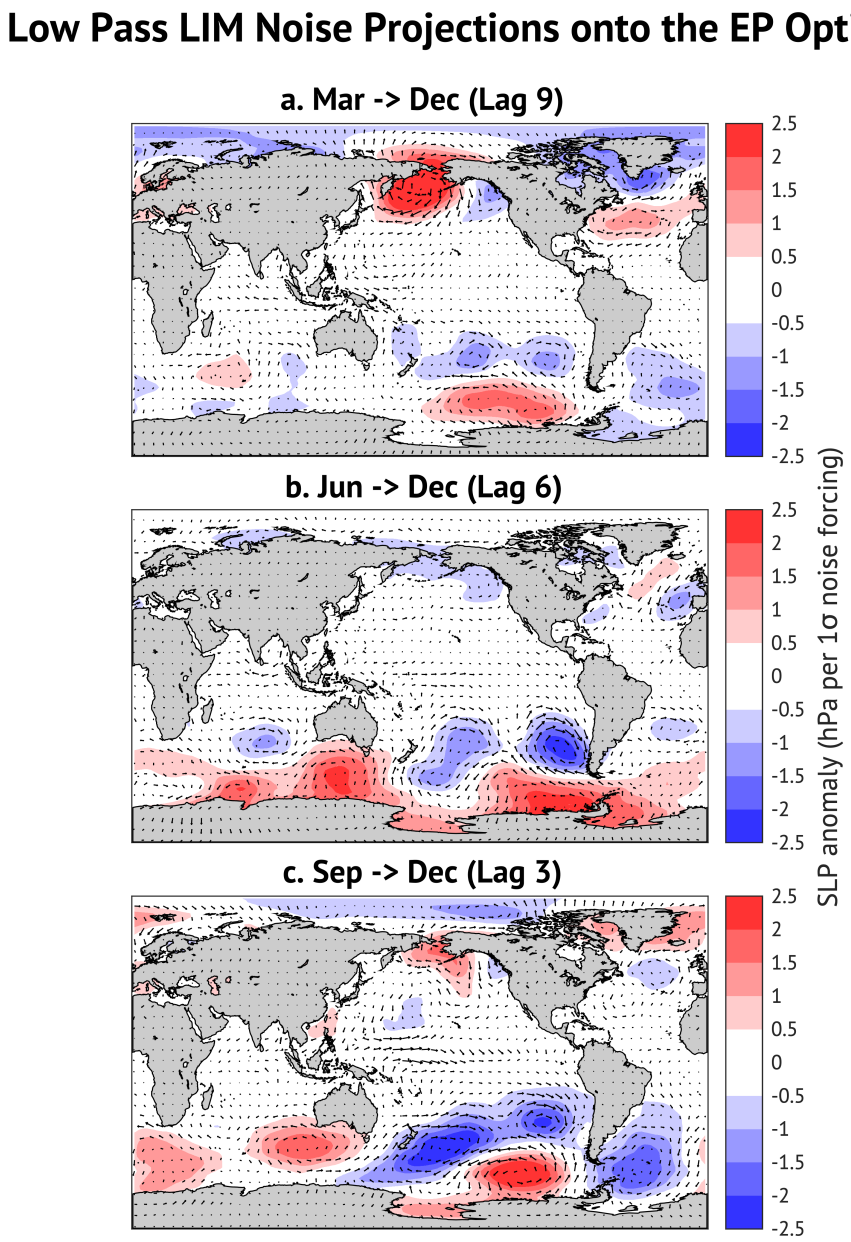

FIGURE 3.12: As in Fig. 3.10 but for the EP optimal.

The spatial regression maps for the CSLIM noise show many similarities with the LIM noise. The NPO structure is present in March (Fig. 3.13a), along with the south Pacific dipole. Weak equatorial westerly wind anomalies are also present in the west Pacific. The NPO disappears in June (Fig. 3.13b), and there is weak Rossby wave activity in the Southern Hemisphere but its signal is not as strong compared to the LIM (Fig. 3.10b). In addition, the equatorial westerly wind is much stronger compared to the LIM. Finally, in September (Fig. 3.13c), there is the South Pacific dipole of SLP, and the equatorial westerly wind anomalies are still present.

The CSLIM noise structures for the CP optimal can also be explained similarly to the LIM noise. However, the June (Fig. 3.14b) and September (Fig. 3.14c) SLP structures in the Southern Hemisphere have a weaker magnitude compared to the LIM.

Finally, the EP structures for the CSLIM can once again be explained similarly to the LIM at all months. However, a difference between the LIM and CSLIM noise structures is the equatorial wind anomalies in June (Figs. 3.12b, 3.15b) and September (Figs. 3.12c, 3.15c). The winds are much more prominent in the LIM structures compared to the CSLIM, and likely reflects the LIM aliasing ENSO's seasonal evolution as noise.

In summary, the noise structures for both the LIM and CSLIM are very similar. Noise structures in mid-latitudes have largest amplitude during austral and boreal winter time. The L2 and CP SLP structures both show structures that are similar to the NPO during March, and disappear in June. CP structures starting in June show Rossby wave train activity in the Southern Hemisphere, with a dominant low pressure signal off the South

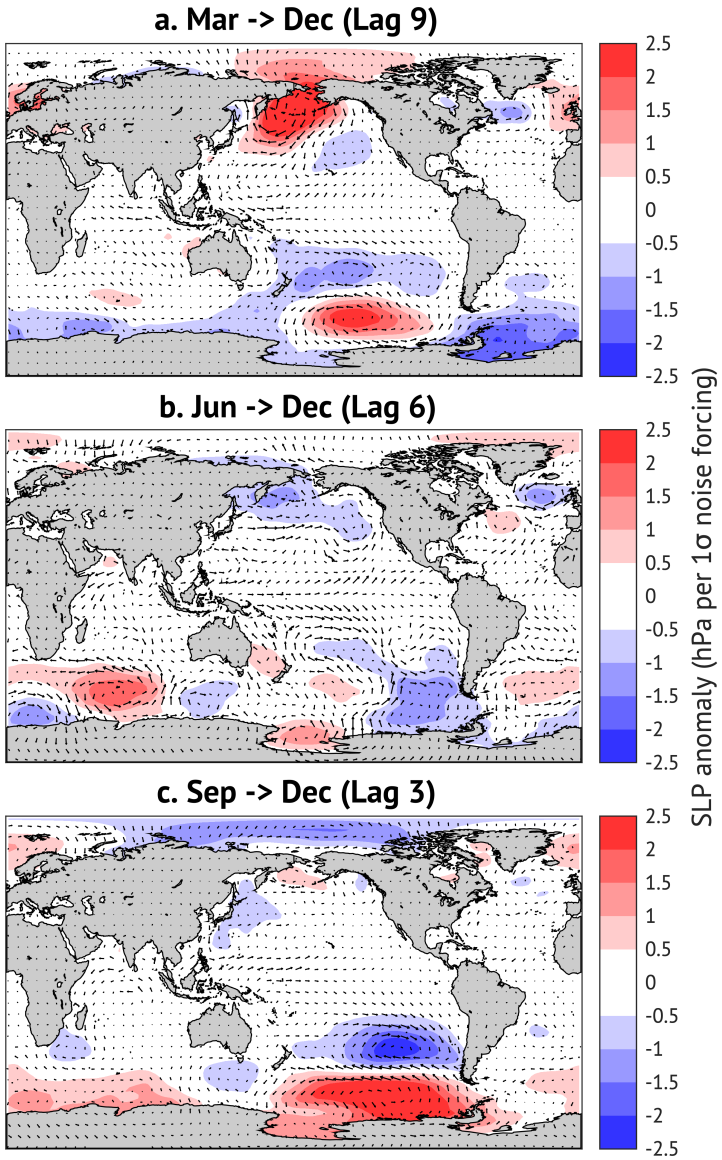

FIGURE 3.13: Spatial maps of the low pass L2-projected estimated CSLIM noise regressed onto SLP (contours) and 10m u and v winds (wind vectors) during (a) March, (b) June, and (c) September where December is the final state.

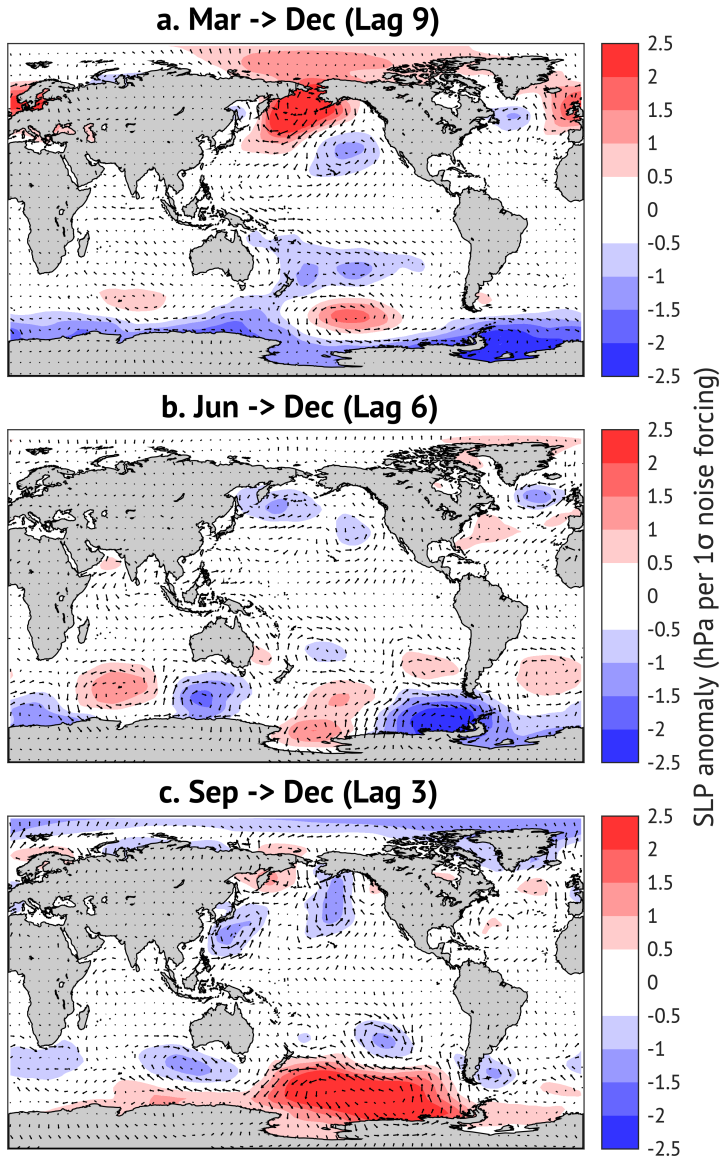

FIGURE 3.14: As in Fig. 3.13, but for the CP optimal.

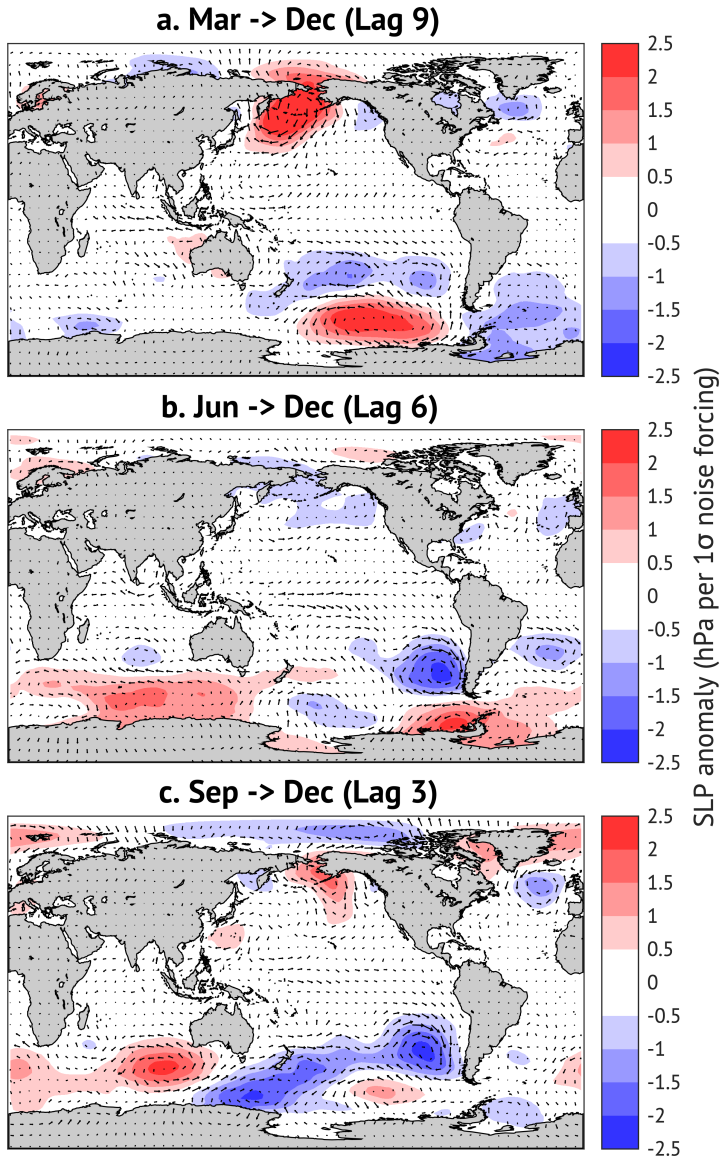

FIGURE 3.15: As in Fig. 3.13 but for the EP optimal.

American coast. EP structures also show wave activity in the Southern Hemisphere, but there is a South Pacific dipole that is similar to the South Pacific Oscillation (You and Furtado (2018)). Equatorial westerly wind anomalies were more present and relatively stronger in the LIM than the CSLIM, and are more apparent at shorter lead times, which is another indicator of the LIM's aliasing ENSO's seasonal development as noise.

3.2.2 Removal of Noise

To further investigate the role of noise forcing within the model framework, the LIM and CSLIM are integrated forward from 1993 to 2022. Figs. 3.17 and 3.19 are constructed by first running the models with the *observed* noise (which, by construction, reproduces the historical evolution; see Fig. 3.17a and 3.19a).

Sensitivity experiments are then performed by rerunning the model while setting the noise forcing to zero during a selected month. The resulting difference between the full evolution and the simulation with noise removed indicates the role of noise forcing in the evolution of the ensuring ENSO event. It is important to note that we are quantifying the sensitivity of the modeled evolution to noise forcing during that month, rather than implying a direct causal influence in the real system.

The selection of months for noise removal is guided by the time series of the projected noise optimal (for the L2 norm only) for both the LIM and CSLIM, as shown in Fig. 3.16 and Fig. 3.19.

3.2.2.1 Removing Noise During El Niño Years

Fig. 3.17 shows the analysis of removing noise during selected months. Focusing first on 2015, this El Niño event was one of the strongest of the past decade. To identify which months to remove noise, we refer to Fig. 3.16a, which shows the low-pass time series of the projected noise optimals with December as the final state using the L2 norm. The noise

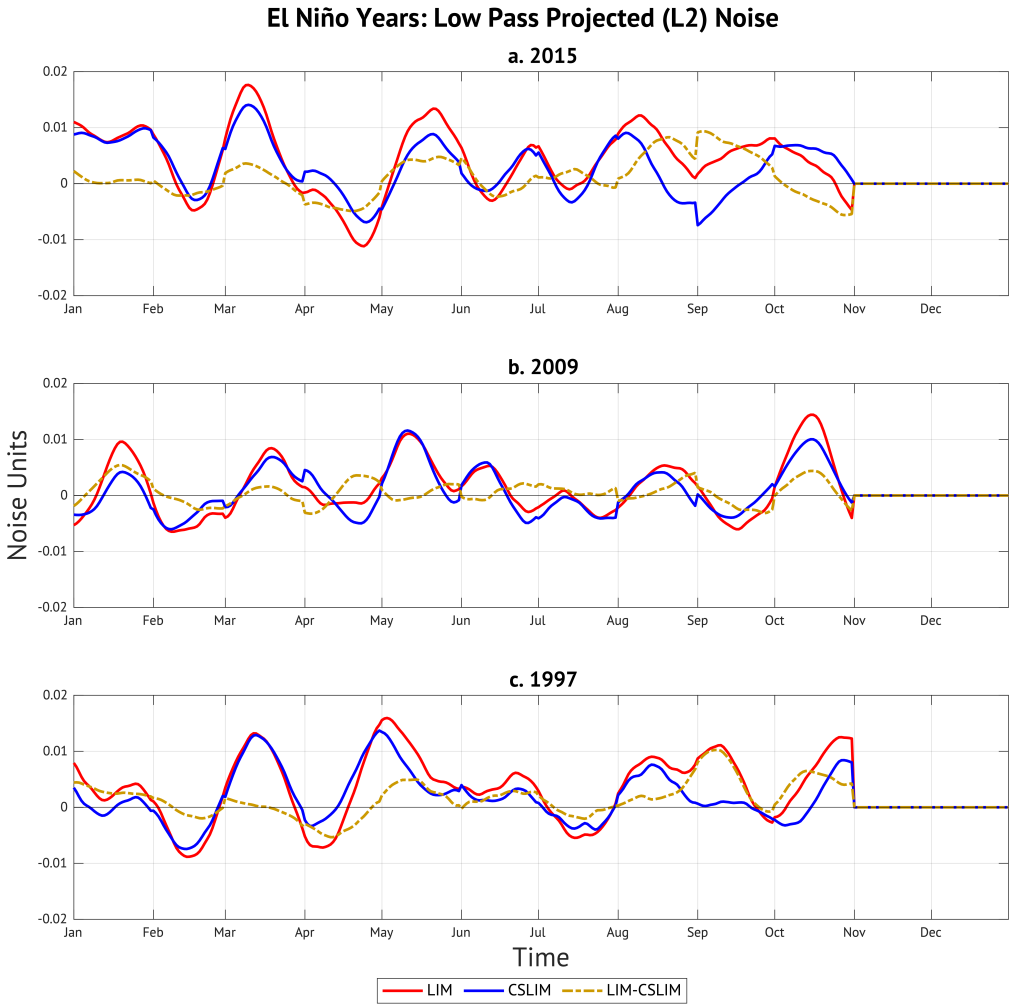

FIGURE 3.16: Low pass time series of the estimated noise projected from the LIM (red) and CSLIM (blue) onto the L2 Optimal shown for (a) 2015, (b) 2009, and (c) 1997. The difference (LIM-CSLIM) is shown in dashed yellow. November (lag 1 month) and December (lag 0 month) values are not considered because December is the final state, which would be the peak of ENSO events. The resulting Niño 3.4 evolution is shown in Fig. 3.17

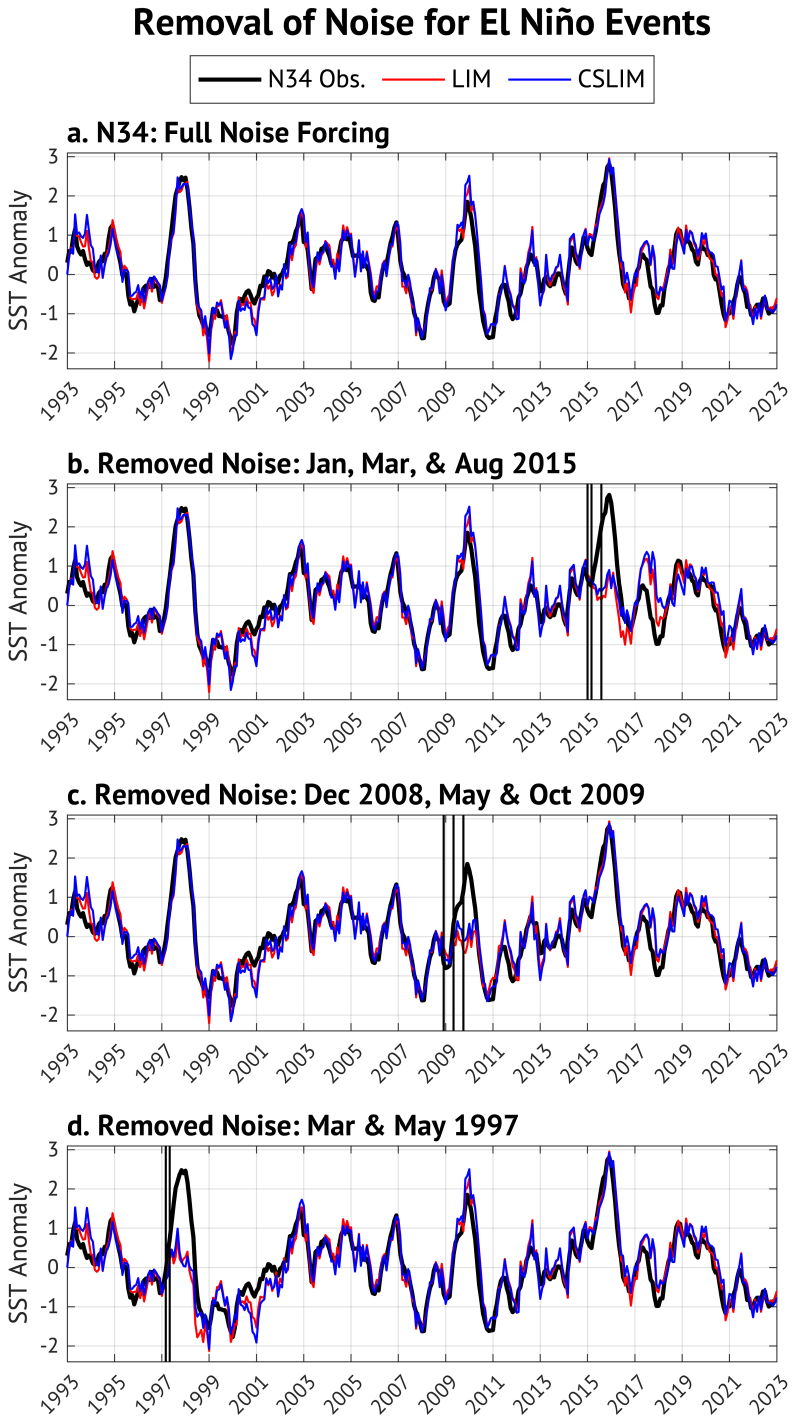

FIGURE 3.17: Various time series of ENSO events using Niño 3.4 from 1993-2023 according to observations (black), the LIM (red), and the CSLIM (blue). (a) shows the full forcing. (b) shows the same time series but removed noise in Jan, Mar, and Aug 2015. The vertical black lines indicate which months were removed. (c) is the removed noise in Dec 2008, May and Oct 2009. (d) is the removed noise in Mar and May 1997.

exhibits clear peaks in March and May for both models. Rerunning the models while removing noise during March and May 2015 results in a significant impact on the event, as shown in Fig. 3.17b. In particular, the 2015 event does not reach its peak amplitude without the noise forcing present during these months, indicating that noise plays a key role in driving the event to its maximum strength. This is consistent with Fig. 3.3, which shows that noise contributes to event development at early lead times. In addition, it is also worth noting the differences in inferred noise forcing during August–September, which are consistent with the Hovmöller diagrams and suggest additional seasonal structure in the noise contribution.

The results for the 2009 CP El Niño event (Fig. 3.17c) can be explained similarly by removing certain months of the noise. In this case, the noise is removed during May and October 2009 because both models have the highest amplitude values shown in Fig. 3.16b. Additionally the noise is removed in December 2008; however, the data in the low pass time series plots end in October. This is because the projected noise optimals all have December as the final state. The November (lag 1 month) and December (lag 0 month) initial states are when ENSO events typically peak, so the values in the time series during these months are omitted. Thus, it can also be said that the 2009 CP El Niño would have not reached its maximum amplitude without the contribution of noise during December 2008, May and October 2009.

Finally, we look at the results for the 1997 El Niño (Fig. 3.17d), which are just as impressive. Fig. 3.16c definitively shows that March and May have the highest noise

amplitudes. When noise forcing during March and May only are removed, both the LIM and CSLIM fail to produce an El Niño event during 1997-98. Interestingly, both the LIM and CSLIM produce persistent La Niña conditions after the event, even without a strong 1997-98 El Niño. This means that the noise forcing that occurred during March and May 1997 were the significant drivers that produced the strong 1997 El Niño. Once again, this is consistent with results found from Fig. 3.3.

The results from this section were able to show that the contribution to noise is important for generating El Niño events. By eliminating noise during certain months for different events, the events themselves would have never reached its maximum amplitude.

3.2.2.2 Removing Noise During La Niña Years

The same analysis is done to different La Niña events as well. Fig. 3.19b shows the simulated evolution of the 1998 and 1999 La Niña events when noise was eliminated from peak of the 1997 El Niño (November 1997) through the following two years (through December 1999). For reference, the low pass time series for the 1998 (Fig. 3.18a) and 1999 (Fig. 3.18b) indicate when the noise should be important; neither shows large negative anomalies, indicating that noise does not appear to be important for the development of the two La Niña years. This is confirmed by removing all noise forcing from November 1997 through December 1999. The resulting Niño 3.4 evolution largely captures the 1998 La Niña (from both the LIM and CSLIM), and the 1999 La Niña (from the CSLIM).

This indicates that conditions leading to the two-year La Niña event were present in the deterministic trajectory at the peak of the 1997 El Niño.

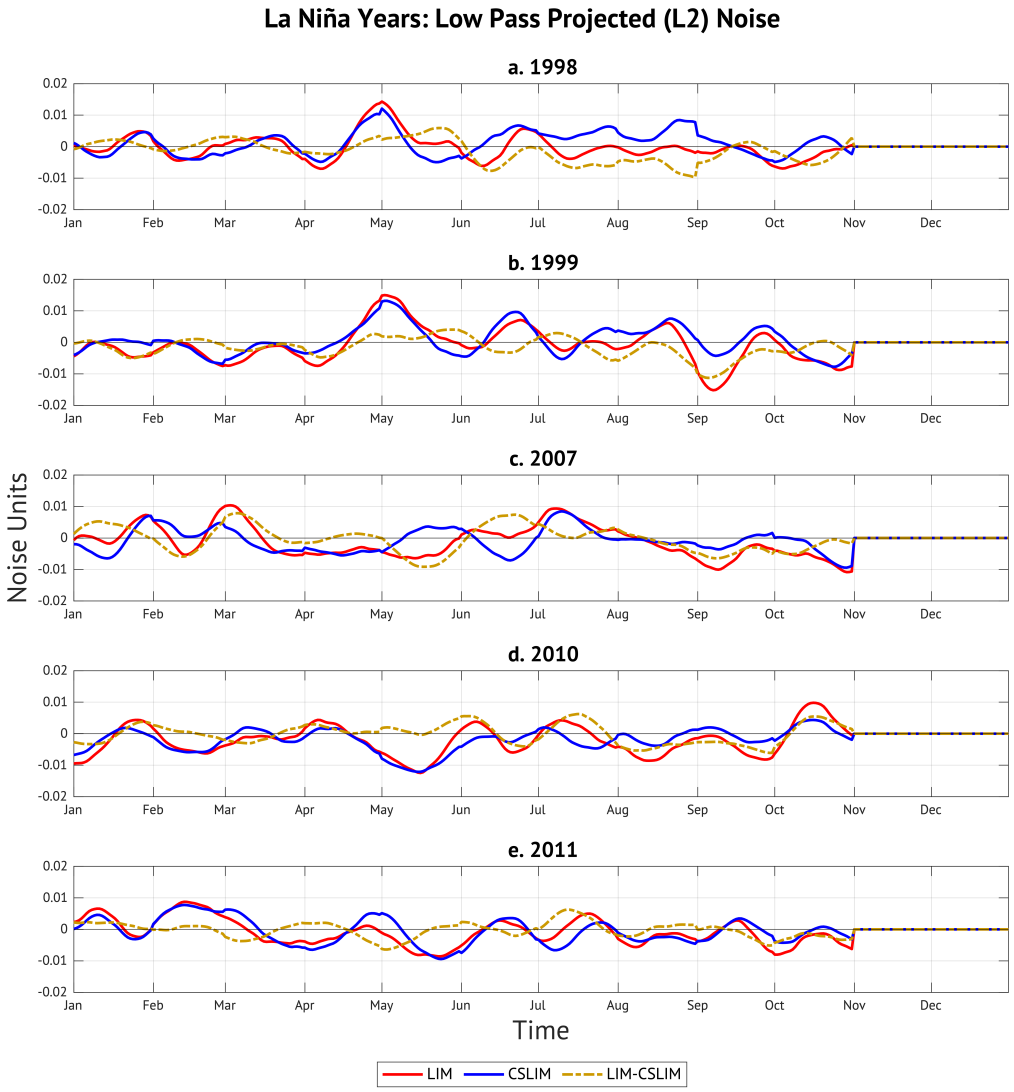

FIGURE 3.18: Low pass time series of the estimated noise projected from the LIM (red) and CSLIM (blue) onto the L2 Optimal during (a) 1998, (b) 1999, (c) 2007, (d) 2010, and (e) 2011. The difference (LIM-CSLIM) is shown in dashed yellow. November (lag 1 month) and December (lag 0 month) values are not considered because December is the final state, which would be the peak of ENSO events. The resulting Niño 3.4 evolution is shown in Fig. 3.19

For the 2007 La Niña, only three months of noise were removed: January, April, and June.

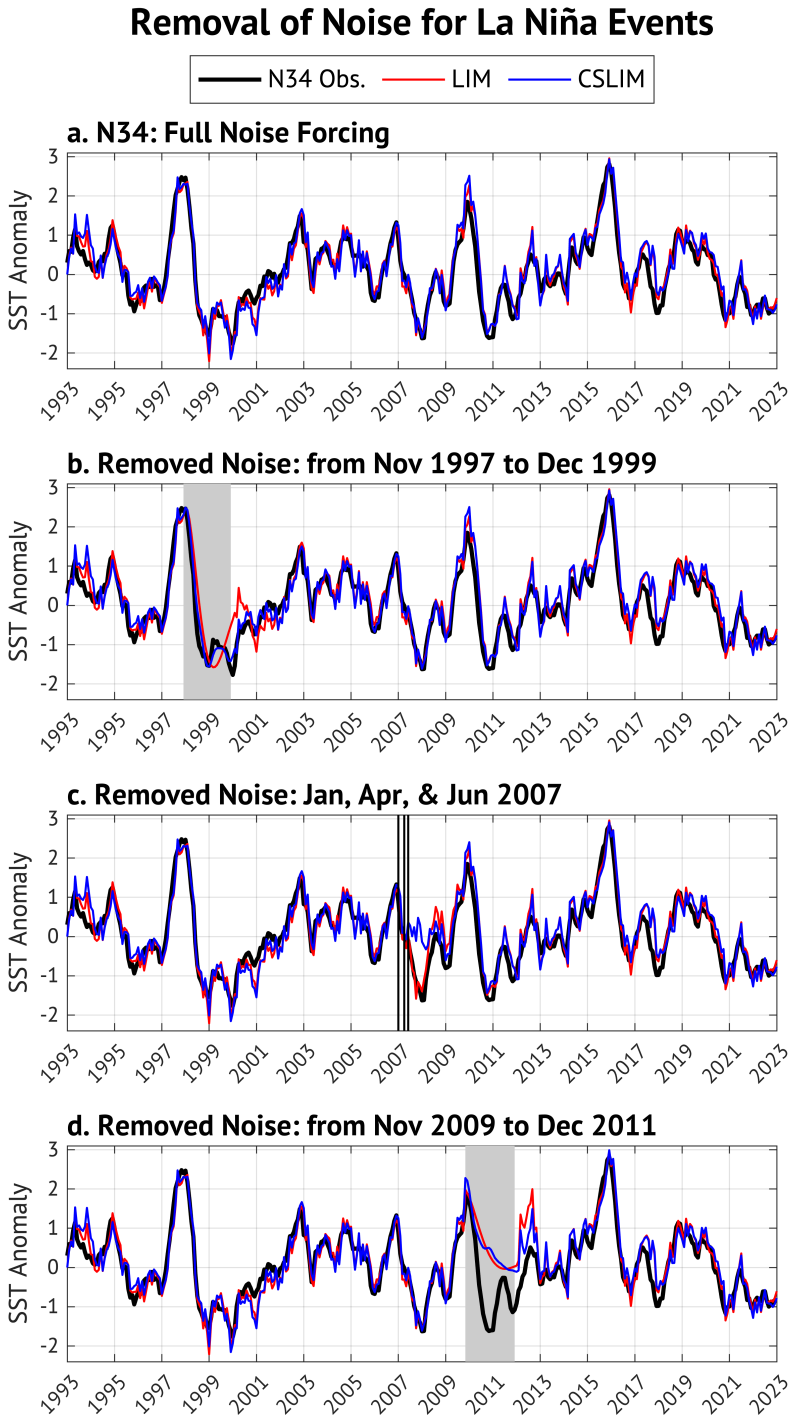

FIGURE 3.19: Same description as 3.17. (a) shows the full forcing. (b) is the removed noise from Nov 1997 to Dec 1999, and the shading indicates the interval of months that the noise was removed. (c) is the removed noise in Jan, Apr, and Jun 2007. The vertical black lines indicate which months removed. (d) is the removed noise from Nov 2009 to Dec 2011.

The results in Fig. 3.19c show that the CSLIM was not able to capture the magnitude of the event, yet the LIM was able to do so. This is because the months chosen for noise removal were based on the low pass time series (Fig. 3.18c). The CSLIM noise is strong during January, April, and June; however these months are not important for the LIM. But, when noise is removed during months the LIM noise has a strong amplitude (February, April, May, and September), then the LIM is not able to capture the La Niña event. Essentially, the time series for this event show a great difference between the LIM and CSLIM noise. By removing certain months that bias towards a model (e.g., LIM), then the impacts of the simulation would show those biases (LIM would not be able to capture the event, but the CSLIM will).

The noise removed for the 2010-2011 (Fig. 3.19d) La Niña is the same for the 1998-1999 event (i.e. the two years following the peak of the preceding El Niño event in 2009; Fig. 3.19b), but the results are drastically different. The time series for both 2010 (Fig. 3.18d) and 2011 (Fig. 3.18e) show that the noise from the LIM and CSLIM have small differences compared to 1998 and 1999. So by removing the noise from November 2009 to Dec 2011, 3.19d shows that both the LIM and CSLIM were not able to capture either the 2010 or 2011 La Niña. One hypothesis to why the 2010-2011 case is different from the 1998-1999 case is that that 2010-2011 followed a CP El Niño, while 1998-1999 followed an EP El Niño. These two types of El Niño events are known to produce different spatial patterns of sea surface temperature anomalies and atmospheric responses, which can strongly influence the subsequent evolution of La Niña (e.g., Ashok et al. (2007), Takahashi et al. (2011)). In particular, CP El Niño events tend to have weaker thermocline feedbacks

and a more westward-shifted anomaly structure compared to EP events, which can lead to a more distributed and less coherent ocean–atmosphere coupling during the transition into La Niña conditions (Zhu et al. (2021)). As a result, the 2010–2011 La Niña could exhibit a more complicated or less dominant signal relative to the background variability, making both the LIM and CSLIM more sensitive to noise removal choices. In contrast, the 1998–1999 La Niña followed a strong EP El Niño which is typically associated with a clearer basin-wide signal. This could make the system more robust to noise removal, allowing at least one of the models to retain predictive skill even when similar amounts of noise are removed.

In a more broad sense, this suggests that ENSO diversity, particularly differences in precursor state and event type, plays a critical role in determining how sensitive model simulations are to noise structure.

Chapter 4

Conclusions & Discussion

This study furthers the results from Thomas et al. (2018) by investigating ENSO dynamics using both the Linear Inverse Model (LIM) and the Cyclostationary Linear Inverse Model (CSLIM), with the goal of evaluating how well each framework represents ENSO evolution. A key distinction between the two approaches is that the CSLIM explicitly incorporates ENSO's seasonal dependence through the construction of seasonally varying dynamics, whereas the LIM relies on stationary dynamics that do not evolve through the seasonal cycle.

The impact of these structural differences is evident in Section 3.1, which examined ENSO evolution using Hovmöller diagrams. For both El Niño and La Niña composites, the CSLIM more accurately captures the seasonally dependent development of ENSO at early lead times and the decay of the event after it peaks in the late calendar year. In

contrast, the LIM primarily reproduces ENSO growth only at lead times near the event peak and does not capture event decay until short lead times. This demonstrates that the LIM misrepresents seasonally varying growth and decay as noise forcing. For individual ENSO events, analysis of March–July initial states further indicates that, in both models, noise plays a substantial role in event development. This motivates the second half of the results, in which the noise term in each model is examined in greater detail.

To investigate the noise forcing, the "observed" noise forcing was inferred by applying the method of Penland and Hartten (2014). In that case, the time tendency of the system is estimated using a centered difference, and the LIM or CSLIM was used as a dynamical filter to remove the deterministic system evolution. The resulting estimated noise forcing was then projected onto a set of optimal structures (L2, CP, and EP), with December as the final state to obtain a time series of the "optimal ENSO forcing". Spatial patterns associated with the noise were subsequently identified by regressing the projected noise time series onto SLP and surface wind anomalies. Distinct structures emerge at different times of year in both frameworks, including an NPO-like pattern in March, Rossby wave train signatures in June, and a South Pacific dipole in September. However, the CSLIM patterns are generally weaker in magnitude than those derived from the LIM. Analysis of the noise variability also provides additional evidence that the LIM aliases seasonally dependent dynamics as noise.

Finally, noise removal experiments were conducted to assess which months contribute most strongly to the development of specific ENSO events. Both the LIM and CSLIM

were integrated forward, with the experiments consisting of selectively removing the noise forcing during particular months for targeted ENSO years, based on the low-pass filtered noise time series. The results demonstrate that removing only a small number of months of stochastic forcing substantially reduces event amplitude, such that strong El Niño events (1997, 2009, and 2015) would not have reached their observed peak magnitude without noise contributions during key periods. The results for La Niña events are more nuanced, particularly for multi-year episodes. When two years of noise forcing were removed, the CSLIM retained the 1998–2000 event more effectively than the LIM, which primarily captured only the 1998 portion. In contrast, for the 2010–2012 event, neither model was able to reproduce the observed evolution under noise removal. These findings support the hypothesis that the character of the preceding El Niño influences the subsequent development of multi-year La Niña events, with the 1997 event representing an EP-type El Niño prior to the 1998–2000 La Niña, and the 2009 event representing a CP-type El Niño prior to the 2010–2012 La Niña.

Ultimately, the results found in this study suggest that ENSO predictability cannot be understood solely through the lens of initial conditions. Instead, event evolution depends strongly on when stochastic forcing occurs and how efficiently that forcing projects onto dynamically relevant structures. By explicitly diagnosing the noise term, this work provides additional insight into the mechanisms underlying ENSO diversity, including the emergence of extreme events and the persistence of multi-year episodes. Continued development of seasonally aware frameworks may therefore offer a more physically consistent basis for interpreting ENSO predictability across timescales.

Bibliography

Ashok, K., S. Behera, S. Rao, H. Weng, and T. Yamagata, 2007: El Niño Modoki and its possible teleconnection. *J. of Geophys. Res.*, **112**, C11007, doi:https://doi.org/10.1029%2F2006JC003798.

Battisti, D., 1988: Dynamics and Thermodynamics of a Warming Event in a Coupled Tropical Atmosphere-Ocean Model. *J. Climate*, **45**, 2889–2919, doi:https://doi.org/10.1175/1520-0469(1988)045<2889:DATOAW>2.0.CO;2.

Battisti, D. and A. Hirst, 1989: Interannual Variability in a Tropical Atmosphere–Ocean Model:. *J. of Atm. Sci.*, **530**, 1687–1712, doi:https://doi.org/10.1175/1520-0469(1989)046%3C1687:IVIATA%3E2.0.CO;2.

Bjerknes, J., 1969: Atmospheric Teleconnections from the Equatorial Pacific. *J. Climate*, **97**, 163–172, doi:https://doi.org/10.1175/1520-0493(1969)097<0163:ATFTEP>2.3.CO;2.

Brooks, C. and H. Braby, 1921: The clash of the trades in the pacific. doi:https://doi.org/10.1002/qj.49704719701.

(C3S), C. C. C. S., 2017: Fifth generation of ECMWF atmospheric reanalyses of the global climate. *Copernicus Climate Change Service Climate Data Store (CDS)*, doi:https://cds.climate.copernicus.eu/cdsapp!/home.

Capotondi, A., A. Wittenberg, M. Newman, E. Di Lorenzo, J. Yu, P. Braconnot, J. Cole, B. Dewitte, B. Giese, E. Guilyardi, F. Jin, K. Karnauskas, B. Kirtman, T. Lee, N. Schneider, Y. Xue, and S. Yeh, 2015: Understanding ENSO Diversity. *Bulletin of the American Meteorological Society*, **96**, 921–938, doi:https://doi.org/10.1175/BAMS-D-13-00117.1.

Chang, P., R. Saravan, T. DelSole, and F. Wang, 2003: Predictability of Linear Coupled Systems: Part I: Theoretical Analyses. *J. Climate*, **17**, 1474–1486, doi:https://doi.org/10.1175/1520-0442(2004)017%3C1474:POLCSP%3E2.0.CO;2.

Deser, C., A. Phillips, R. Tomas, Y. Okumura, M. Alexander, A. Capotondi, J. Scott, Y. Kwon, and M. Ohba, 2012: ENSO and Pacific Decadal Variability in the Community Climate System Model Version 4. *J. Clim.*, **25**, 2622–2651, doi:https://doi.org/10.1175/JCLI-D-11-00301.1.

Enfield, D., 1989: EL NINO , PAST AND PRESENT. *Reviews of Geophysics*, **27**, 159–187.

Gill, A. and E. M. Rasmusson, 1983: The 1982-83 Climate Anomaly in the Equatorial Pacific. *Nature*, **306**, 229–234, doi:https://doi.org/10.1038/306229a0.

Hasselman, K., 1976: Stochastic climate models Part I. Theory. *Tellus*, **28**, 473–485, doi:https://doi.org/10.3402/tellusa.v28i6.11316.

Huang, B., C. Liu, V. Banzon, E. Freeman, G. Graham, B. Hankins, T. Smith, and H.-M. Zhang, 2021: Improvements of the Daily Optimum Interpolation Sea Surface Temperature (DOISST) Version 2.1. *J. Climate*, **34**, 2923–2939, doi:10.1175/JCLI-D-20-0166.1.

Huang, B., P. Thorne, V. Banzon, T. Boyer, G. Chepurin, J. Lawrimore, M. Menne, T. Smith, R. Vose, and H.-M. Zhang, 2017: Extended Reconstructed Sea Surface Temperature version 5 (ERSSTv5), Upgrades, validations, and intercomparisons. *J. Climate*, **30**, 8179–8205, doi:10.1175/JCLI-D-16-0836.1.

Ichiye, T. and J. Peterson, 1963: The anomalous rainfall of the 1957-58 winter in the equatorial central Pacific arid area. *J. Meteorology Society of Japan*, **41**, 172–182.

Leighly, J., 1933: Marquesan Meteorology, 147–172.

Lellouche, J., E. Greiner, R. Bourdallé-Badie, G. Garric, A. Melet, M. Drévillon, C. Bricaud, M. Hamon, O. Le Galloudec, C. Regnier, T. Candela, C. Testut, F. Gasparin, G. Ruggiero, M. Benkiran, Y. Drillet, and P. Le Traon, 2021: The Copernicus Global 1/12° Oceanic and Sea Ice GLORYS12 Reanalysis. *CFront. Earth Sci.*, doi:https://doi.org/10.3389/feart.2021.698876.

Linkin, M. and S. Nigam, 2008: The North Pacific Oscillation–West Pacific Teleconnection Pattern: Mature-Phase Structure and Winter Impacts. *J. Clim.*, **21**, 1979–1997, doi:https://doi.org/10.1175/2007JCLI2048.1.

McPhaden, M., S. Zebiak, and M. Glantz, 2006: Enso as an integrating concept in earth science. *Science*, **314**, 1740–1745, doi:10.1126/science.1132588.

Murphy, R., 1923: The Oceanography of the Peruvian Littoral with Reference to the Abundance and Distribution of Marine Life. *Geographical Review*, **13**, 64–85.

— 1926: Oceanic and Climatic Phenomena along the West Coast of South America during 1925. *Geographical Review*, **16**, 26–54.

Neelin, J., D. Battisti, A. Hirst, F. Jin, Y. Wakata, T. Yamagata, and S. Zebiak, 1998: ENSO Theory. *J. Geophys. Res*, **103**, 14261–14290, doi:https://doi.org/10.1029/97JC03424.

Newman, M. and P. Sardeshmukh, 2017: Are we near the predictability limit of tropical Indo-Pacific sea surface temperatures? *Geophys. Res. Lett.*, **44**, 8520–8529, doi:https://doi.org/10.1002/2017GL074088.

Penland, C. and L. Hartten, 2014: Stochastic forcing of north tropical Atlantic sea surface temperatures by the North Atlantic Oscillation. *Geophys. Res. Lett.*, **41**, 2126–2131, doi:https://doi.org/10.1002/2014GL059252.

Penland, C. and L. Matrasova, 1994: A Balance Condition for Stochastic Numerical Models with Application to the El Niño-Southern Oscillation. *J. Climate*, **7**, 1352–1372, doi:https://doi.org/10.1175/1520-0442(1994)007%3C1352:ABCFSN%3E2.0.CO;2.

Penland, C. and P. Sardeshmukh, 1995: The Optimal Growth of Tropical Sea Surface Temperatures. *J. Climate*, **8**, 1999–2004, doi:/https://doi.org/10.1175/1520-0442(1995)008%3C1999:TOGOTS%3E2.0.CO;2.

Philander, G., 1990: El nino, la nina, and the southern oscillation. *Academic Press*, **46**.

Picaut, J., F. Masia, and Y. du Penhoat, 1997: An advective-reflective conceptual model for the oscillatory nature of the ENSO. *Science*, **277**, 663–666.

Shin, S.-I., P. Sardeshmukh, M. Newman, C. Penland, and M. Alexander, 2021: Impact of Annual Cycle on ENSO Variability and Predictability. *J. Climate*, **34**, 171–193, doi:10.1175/JCLI-D-20-0166.1.

Suarez, M. and P. Schopf, 1988: A Delayed Oscillator for ENSO. *J. Atmospheric Sciences*, **45**, 3283–3287, doi:https://doi.org/10.1175/1520-0469(1988)045%3C3283:ADAOFE%3E2.0.CO;2.

Takahashi, K., A. Montecinos, G. K., and B. Dewitte, 2011: ENSO regimes: Reinterpreting the canonical and Modoki El Niño. *Geophys. Res. Lett.*, **38**, 7129–7132, doi:http://dx.doi.org/10.1029/2011GL047364.

Thomas, E., D. Vimont, M. Newman, and C. Martinez-Villalobos, 2018: The Role of Stochastic Forcing in Generating ENSO Diversity. *J. Climate*, **31**, 9125–9150, doi:https://doi.org/10.1175/JCLI-D-17-0582.1.

Trenberth, K., G. Branstator, D. Karoly, A. Kumar, N. Lau, and C. Ropelewski, 1998: Progress during TOGA in understanding and modeling global teleconnections associated with tropical sea surface temperatures. *J. Geophys. Res.*, **103**, 14291–14324, doi:https://doi.org/10.1029/97JC01444.

Tziperman, E., L. Zanna, and C. Penland, 2008: Nonnormal Thermohaline Circulation Dynamics in a Coupled Ocean–Atmosphere GCM. *J. Physical Oceanography*, **38**, 588–604, doi:https://doi.org/10.1175/2007JPO3769.1.

Vimont, D., M. Alexander, and M. Newman, 2014: Optimal Growth of Central and East Pacific ENSO Events. *Geophys. Res. Lett.*, **41**, 4027–4034, doi:http://dx.doi.org/10.1002/2014GL059997.

Vimont, D., M. Newman, D. Battisti, and S.-I. Shin, 2022: The Role of Seasonality and the ENSO Mode in Central and East Pacific ENSO Growth and Evolution. *J. Climate*, **35**, 3195–3209, doi:10.1175/JCLI-D-21-0599.1.

Walker, G., 1925: CORRELATION IN SEASONAL VARIATIONS OF WEATHER—A FURTHER STUDY OF WORLD WEATHER. *Monthly Weather Review*, **53**, 252–254, doi:https://doi.org/10.1175/1520-0493(1925)53%3C252:CISVOW%3E2.0.CO;2.

Wallace, J., E. Rasmusson, T. Mitchell, K. V.E., E. Sarachik, and H. von Storch, 1998: On the structure and evolution of ENSO-related climate variability in the tropical Pacific: Lessons from TOGA. *J. Geophys. Res.*, **103**, 14241–14259, doi:https://doi.org/10.1029/97JC02905.

Wang, C., C. Deser, Y. J., P. DiNezio, and A. Clement, 2017: El Niño and Southern Oscillation (ENSO): A Review. *Coral Reefs of the Eastern Tropical Pacific*, 85–106, doi:10.1007/978-94-017-7499-4_4.

Wang, C., W. R.H., and V. J.I., 1999: Western Pacific interannual variability associated with the El Niño-Southern Oscillation. *J. Geophys. Res.*, **104**, 5131–5149, doi:http://dx.doi.org/10.1029/147GM02.

Wyrtki, K., 1975: El Niño—the dynamic response of the equatorial Pacific Ocean to atmospheric forcing. *J. of Phys. Oceanography*, **5**, 572–584, doi:https://doi.org/10.1175/1520-0485(1975)005%3C0572:ENTDRO%3E2.0.CO;2.

— 1985: Water displacements in the Pacific and the genesis of El Niño cycles. *J. Geophys. Res.*, **90**, 7129–7132, doi:https://doi.org/10.1029/JC090iC04p07129.

You, Y. and J. Furtado, 2018: The South Pacific Meridional Mode and Its Role in Tropical Pacific Climate Variability. *J. Clim.*, **31**, 10141–10163, doi:https://doi.org/10.1175/JCLI-D-17-0860.1.

Zebiak, S. and M. Cane, 1987: A Model El Niño-Southern Oscillation. *Monthly Weather Review*, **115**, 2262–2278, doi:https://doi.org/10.1175/1520-0493(1987)115%3C2262:AMENO%3E2.0.CO;2.

Zhu, X., S. Chen, R. Greatbatch, M. Claus, and J. Xing, 2021: Role of thermocline feedback in the increasing occurrence of Central Pacific ENSO. *Regional Studies in Marine Science*, **41**, doi:https://doi.org/10.1016/j.rsma.2020.101584.

Zuo, H., M. Balmaseda, S. Tietsche, K. Mogensen, and M. Mayer, 2019: The ECMWF operational ensemble reanalysis–analysis system for ocean and sea ice: a description of the system and assessment. *Ocean Sci.*, **15**, 779–808, doi:https://doi.org/10.5194/os-15-779-2019.